Optimal Multiharmonic Forcing Design for Homoclinic Chaos Control via Convex Optimization

Víctor M. Preciado
Department of Electrical and Systems Engineering, University of Pennsylvania
Philadelphia, PA, USA · preciado@seas.upenn.edu

Abstract

Small periodic perturbations can split a homoclinic orbit and produce transverse intersections between the stable and unstable manifolds of a saddle. We design phase-locked multiharmonic forcing to prevent these crossings near a specified orbit for sufficiently small perturbations. The design maximizes the uniform distance of the first-order Melnikov function from zero under a power budget, or minimizes the power required for a prescribed margin. For a finite harmonic drive, the Melnikov function is a trigonometric polynomial whose coefficients depend affinely on the sine and cosine control amplitudes. The Fejér–Riesz theorem gives an exact semidefinite certificate for its sign over all forcing phases. In a Helmholtz escape oscillator, we prove that control at the fundamental frequency has a sharp margin ceiling of approximately 0.0355 at any power. Adding the second harmonic makes a margin of 0.08 attainable. For a Duffing resonator and a Josephson junction, multiharmonic control reduces power by 27% and 7%, respectively, at matched margins certified on both homoclinic branches. Nonlinear simulations assess the finite-perturbation response through manifold tracing, periodic-orbit diagnostics, and finite-horizon escape tests.

Keywords. chaos control, Melnikov method, semidefinite programming, multiharmonic forcing, homoclinic bifurcation, nonlinear oscillators

Graphical abstract

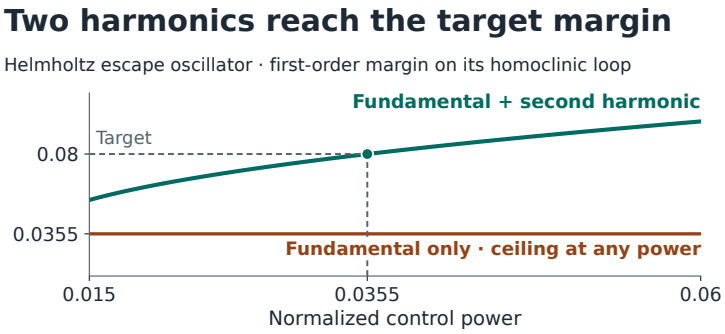

1 Introduction

Nonlinear oscillators in engineering applications frequently operate under perturbations that cannot be eliminated, arising from operational requirements, environmental disturbances, or inherent coupling with external fields. When these perturbations drive the system into a chaotic regime, a natural question arises: can supplementary forcing be designed, within realistic actuator constraints, to suppress or manage the chaotic dynamics without requiring real-time state feedback?

The classical Melnikov method [1, 2] provides a criterion for predicting transverse intersections of the stable and unstable manifolds of a hyperbolic saddle under small perturbations of planar

Hamiltonian systems. Simple zeros of the Melnikov function $\mathcal{M}(t_0)$ correspond to transverse intersections of the stable and unstable manifolds, and by the Smale–Birkhoff theorem [2, 3] this transversality implies the existence of a horseshoe and, hence, chaotic invariant sets. When $\mathcal{M}(t_0)$ has a uniform definite sign, crossings near the selected homoclinic orbit are excluded for sufficiently small ε. Other routes to chaos are outside this criterion. This geometric insight has motivated a substantial literature on chaos control through open-loop forcing design.

Early work by Lima and Pettini [4] demonstrated that a single additional harmonic can suppress chaos in a parametrically driven system, and Braiman and Goldhirsch [5] showed similar effects in the Duffing oscillator. Chacón [6, 7] developed a systematic theory of subharmonic and ultrasubharmonic resonances for chaos suppression, establishing analytical conditions on forcing amplitudes and phases. In parallel, feedback-based methods emerged: Ott, Grebogi, and Yorke [8] introduced small parameter perturbations to stabilize unstable periodic orbits within an existing chaotic attractor, Pyragas [9] proposed continuous delayed feedback control targeting periodic orbits of known period, and Shinbrot et al. [10] provided an accessible review of these approaches.

Several earlier studies bear directly on multiharmonic open-loop design. Preciado and Chacón [11] expressed Melnikov suppression conditions in polynomial form and used root-locus analysis to identify ranges of forcing parameters that suppress homoclinic chaos. Chacón, Preciado, and Tereshko [12] studied suppression by multiple weak resonant excitations, including applications to arrays of coupled oscillators. The NOLCOS 2004 program lists a contribution by Preciado and Verghese [13] on multiharmonic inputs for homoclinic chaos suppression using Melnikov analysis and root-locus design. Lenci and Rega optimized superharmonic forcing to delay homoclinic bifurcation in Duffing [14] and Helmholtz [15] oscillators. Cao and Chen [16] also studied the control of homoclinic and heteroclinic bifurcations. The relative phase of an added harmonic can itself promote or suppress chaos [17], an effect studied in experiments on intermittency [18].

Here we consider a finite set of harmonics locked to the existing drive. The design objective is to maximize the minimum signed first-order Melnikov margin over forcing phase for a given control-power budget, or to minimize the power needed for a prescribed margin. The sine and cosine control coefficients enter the Melnikov polynomial affinely. Applying the Fejér–Riesz theorem to that polynomial with the required sign and margin gives an exact semidefinite constraint for all phases. The two semidefinite programs therefore optimize the first-order margin or the control power over the entire admissible harmonic basis. A separate constraint for each protected branch lets the same waveform certify both branches. Section 7.4 compares the convex formulation with Lenci and Rega's published Helmholtz gains.

Section 3 derives the Fourier coefficients from orbit integrals and gives the matrix constraints for the two design problems. We apply the formulation to a MEMS-inspired Duffing resonator (Section 5), a Josephson junction (Section 6), and a Helmholtz escape oscillator (Section 7). In the Duffing and Josephson examples we compare power at matched two-branch margins. In the single-loop Helmholtz example, two harmonics yield approximately 2.8 times the fundamental-only margin at the same power and attain a target above the fundamental-only ceiling. Section 3.6 relates these designs to single-harmonic and feedback control. The case studies use nondimensional models.

2 Problem Formulation and Melnikov Design Principle

2.1 Standing hypotheses

Assumption 1. We consider systems of the form

$$\dot{\mathbf{z}} = \mathbf{f}(\mathbf{z}) + \varepsilon\, \mathbf{g}(\mathbf{z}, t), \quad 0 < \varepsilon \ll 1, \tag{1}$$

where $\mathbf{z} = (x, y)$ belongs to the plane $\mathbb{R}^2$ or, for an angular coordinate x modulo 2π, to the cylinder $(\mathbb{R}/2\pi\mathbb{Z}) \times \mathbb{R}$. We assume the following: (*1*) the *unperturbed system* $\dot{\mathbf{z}} = \mathbf{f}(\mathbf{z})$ is Hamiltonian with smooth Hamiltonian $H_0(\mathbf{z})$, so that $\mathbf{f} = J\,\nabla H_0$ with J the standard symplectic matrix; (*2*) the unperturbed system possesses a hyperbolic saddle point $\mathbf{p}$ connected to itself by a single-pulse homoclinic orbit $\mathbf{z}_h(t)$ satisfying $\lim_{t\to\pm\infty} \mathbf{z}_h(t) = \mathbf{p}$; (*3*) the perturbation $\mathbf{g}$ is T-periodic in t with $T = 2\pi/\Omega$ and sufficiently smooth.

Under the perturbation $\varepsilon\,\mathbf{g}(\mathbf{z}, t)$, the stable and unstable manifolds of the saddle, which coincide along the homoclinic orbit in the unperturbed system, generically split apart. The Melnikov function measures this separation to first order in ε [1, 2, 19].

Definition 1 (Melnikov function)**.** The first-order Melnikov function for (1) is

$$\mathcal{M}(t_0) := \int_{-\infty}^{\infty} \omega\Big(\mathbf{f}(\mathbf{z}_h(t)),\, \mathbf{g}(\mathbf{z}_h(t), t + t_0)\Big)\,dt, \tag{2}$$

where $\omega = dx \wedge dy$ is the standard area form in these coordinates, with $\omega((\alpha_1, \alpha_2), (\beta_1, \beta_2)) = \alpha_1\beta_2 - \alpha_2\beta_1$. This expression is invariant under $x \mapsto x + 2\pi$ on the cylinder.

Simple zeros of $\mathcal{M}(t_0)$ correspond to transverse intersections of the stable and unstable manifolds at first order in ε; by the Smale–Birkhoff theorem [1–3], such intersections imply the existence of chaotic invariant sets for sufficiently small ε. When $\mathcal{M}(t_0)$ is bounded away from zero, the leading splitting has a definite sign. We use *suppression* to mean exclusion of the selected local homoclinic crossings in this perturbative sense, and assess finite-ε dynamics separately.

2.2 Multiharmonic forcing structure

We consider multi-harmonic perturbations with a finite Fourier representation:

$$\begin{aligned}\mathbf{g}(\mathbf{z}, t) = \mathbf{g}_0(\mathbf{z}) + \sum_{k=1}^{N} \big[&\mathbf{g}_k^c(\mathbf{z}) \cos k\Omega t \\ &+ \mathbf{g}_k^s(\mathbf{z}) \sin k\Omega t\big],\end{aligned} \tag{3}$$

where $\Omega > 0$ is the fundamental frequency, N is the number of harmonics, and the vector fields $\mathbf{g}_k^c, \mathbf{g}_k^s$ encode the spatial distribution of each component. This structure captures a broad class of realizable forcing protocols while maintaining analytical tractability: the finite Fourier structure leads to Melnikov functions that are trigonometric polynomials.

3 Fourier Representation and Convex Synthesis Framework

Since $\mathcal{M}(t_0)$ is T-periodic in t_0, we introduce the normalized phase $\theta := \Omega t_0$ and write $\mathcal{M}(\theta)$ throughout.

3.1 Melnikov–Fourier representation

Theorem 1 (Melnikov–Fourier representation)**.** *Under multiharmonic forcing* (3)*, the Melnikov function admits the exact trigonometric polynomial representation*

$$\mathcal{M}(\theta) = c_0 + \sum_{k=1}^{N} \left(c_k \cos k\theta + d_k \sin k\theta\right), \tag{4}$$

where the Fourier coefficients are

$$c_0 = \int_{-\infty}^{\infty} \omega\big(\mathbf{f}(\mathbf{z}_h),\, \mathbf{g}_0(\mathbf{z}_h)\big)\, dt, \tag{5}$$

$$c_k = \int_{-\infty}^{\infty} \big[w_k^c(t)\cos k\Omega t + w_k^s(t)\sin k\Omega t\big]\, dt, \tag{6}$$

$$d_k = \int_{-\infty}^{\infty} \big[-w_k^c(t)\sin k\Omega t + w_k^s(t)\cos k\Omega t\big]\, dt. \tag{7}$$

Here $w_k^{c,s}(t) = \omega(\mathbf{f}(\mathbf{z}_h(t)), \mathbf{g}_k^{c,s}(\mathbf{z}_h(t)))$*. All integrals are evaluated along the homoclinic orbit* $\mathbf{z}_h(t)$*.*

Proof. Substituting (3) into (2) and using the trigonometric addition formulas $\cos\big(k\Omega(t+t_0)\big) = \cos(k\Omega t)\cos(k\theta) - \sin(k\Omega t)\sin(k\theta)$ (with $\theta = \Omega t_0$) and analogously for the sine terms, the result follows by collecting coefficients of $\cos k\theta$ and $\sin k\theta$. Convergence of all integrals follows from the exponential decay of $\mathbf{z}_h(t)$ to the saddle $\mathbf{p}$ as $t \to \pm\infty$. □

Each coefficient c_k, d_k represents the resonant response of the homoclinic orbit to the k-th harmonic excitation. The coefficient c_0 captures time-independent effects such as damping or DC bias. The finite-dimensional structure is exact (not an approximation), reducing the infinite-dimensional problem of controlling manifold splitting to manipulating finitely many Fourier coefficients.

3.2 Nonnegativity certificate via the Fejér–Riesz theorem

The central mathematical tool is the following classical result, which provides an exact bridge between global nonnegativity and positive semidefiniteness [20–22].

Theorem 2 (Fejér–Riesz certificate)**.** *The trigonometric polynomial* $\mathcal{M}(\theta) \geq 0$ *for all* $\theta \in [0, 2\pi]$ *if and only if there exists a Hermitian positive semidefinite matrix* $\mathbf{H} \in \mathbb{C}^{(N+1)\times(N+1)}$*,* $\mathbf{H} \succeq 0$*, such that*

$$\mathcal{M}(\theta) = \mathbf{v}(\theta)^* \mathbf{H}\, \mathbf{v}(\theta), \quad \forall\, \theta \in [0, 2\pi], \tag{8}$$

where $\mathbf{v}(\theta) = [1, e^{\mathrm{i}\theta}, \ldots, e^{\mathrm{i}N\theta}]^\top$*. This representation is equivalent to the system of linear constraints*

$$\hat{c}_k = \sum_{j=0}^{N-k} \mathbf{H}_{j,j+k}, \quad k = 0, 1, \ldots, N, \tag{9}$$

relating the complex Fourier coefficients $\hat{c}_k = (c_k - \mathrm{i}d_k)/2$ *(for* $k > 0$*),* $\hat{c}_0 = c_0$*, to the diagonal-offset sums of* $\mathbf{H}$*. Negative-frequency coefficients* $\hat{c}_{-k} = \overline{\hat{c}_k}$ *are handled automatically by the Hermitian symmetry* $\mathbf{H} = \mathbf{H}^*$*.*

By the Fejér–Riesz theorem, a nonnegative trigonometric polynomial of degree N factors as $|p(e^{\mathrm{i}\theta})|^2$ for a polynomial p of degree N. Expanding this product yields the Gram matrix representation (8). The equivalence with the diagonal-offset (i.e., entries of $\mathbf{H}$ that lie along the k-th diagonal above the main diagonal) sum constraints (9) follows by direct computation. A proof sketch is given in Appendix B; see also Dumitrescu [21] and Grenander and Szegő [22] for more details.

There is no gap between the geometric condition (global nonnegativity) and the algebraic certificate (positive semidefinite matrix). The constraints (9) are linear in the entries of $\mathbf{H}$, requiring that each diagonal-offset sum matches the corresponding Fourier coefficient. The feasible set comprises all Hermitian positive semidefinite matrices satisfying these linear constraints, which is generally larger than the set of Toeplitz matrices since individual entries of $\mathbf{H}$ are free as long as the diagonal-offset sums match.

3.3 Convex synthesis in Cartesian coordinates

In many physical realizations, the designer controls only the amplitude A_k and phase ϕ_k of each harmonic. In this setting, the coefficient fields in (3) take the form

$$\begin{aligned} \mathbf{g}_k^c(\mathbf{z}) &= A_k \cos\phi_k \; \hat{\mathbf{g}}_k(\mathbf{z}), \\ \mathbf{g}_k^s(\mathbf{z}) &= A_k \sin\phi_k \; \hat{\mathbf{g}}_k(\mathbf{z}), \end{aligned} \tag{10}$$

where $\hat{\mathbf{g}}_k(\mathbf{z})$ is the fixed vector field describing how the k-th harmonic couples to the system. The products of amplitudes and trigonometric functions of phase make this parametrization nonconvex. The following Cartesian coefficients remove those products and lead to the convex programs below [23].

$$a_k := A_k \cos\phi_k, \qquad b_k := A_k \sin\phi_k. \tag{11}$$

In terms of the system-specific response kernels κ_k^c, κ_k^s (precomputed from the homoclinic orbit), the Melnikov Fourier coefficients become affine in (a_k, b_k):

$$c_k = a_k \, \kappa_k^c - b_k \, \kappa_k^s, \tag{12}$$

$$d_k = b_k \, \kappa_k^c + a_k \, \kappa_k^s, \tag{13}$$

where the response kernels are defined by

$$\kappa_k^c = \int_{-\infty}^{\infty} \omega(\mathbf{f},\, \hat{\mathbf{g}}_k) \cos(k\Omega t)\, dt, \tag{14}$$

$$\kappa_k^s = -\int_{-\infty}^{\infty} \omega(\mathbf{f},\, \hat{\mathbf{g}}_k) \sin(k\Omega t)\, dt, \tag{15}$$

with all integrals evaluated along the homoclinic orbit $\mathbf{z}_h(t)$. These kernels encode how strongly the homoclinic orbit responds to the k-th harmonic of the forcing; they depend only on the unperturbed system and the coupling geometry $\hat{\mathbf{g}}_k$, and are precomputed once for a given oscillator. We define the normalized control power as $P := \sum_k A_k^2 = \sum_k (a_k^2 + b_k^2)$. For $u(t) = \sum_k [a_k \cos(k\Omega t) + b_k \sin(k\Omega t)]$, Parseval's identity gives $P = 2T^{-1} \int_0^T u(t)^2\, dt$; conversion to physical power requires an actuator model. This power and per-harmonic amplitude bounds $A_k \le A_{k,\max}$ (equivalently $a_k^2 + b_k^2 \le A_{k,\max}^2$), are both convex constraints in the Cartesian variables; a total power control budget $\sum_k A_k^2 \le P_{\max}$ is likewise convex. After solving the optimization problems described below, amplitudes and phases are recovered via $A_k = \sqrt{a_k^2 + b_k^2}$ and $\phi_k = \operatorname{atan2}(b_k, a_k)$.

The Cartesian parametrization, combined with the Fejér–Riesz certificate, yields two canonical control synthesis problems, both convex. In what follows, we define the *suppression margin* as $\tau := \min_\theta(-\mathcal{M}(\theta))$, so that $\tau > 0$ certifies $\mathcal{M}(\theta) < 0$ for all θ and, hence, the absence of first-order homoclinic intersections. The convention $-\mathcal{M}(\theta)$ is natural when $c_0 < 0$, as in all three case studies, where damping contributes a negative constant to $\mathcal{M}$ and the sign-indefinite contribution comes from the periodic forcing.

Problem 1 (Max-margin suppression)**.** Given a power budget $P_{\max}$, find the forcing coefficients (a_k, b_k) that maximize the suppression margin:

$$\max_{a_k, b_k, \tau, \mathbf{H}} \quad \tau \tag{16}$$

$$\text{s.t.} \quad -\mathcal{M}(\theta) - \tau = \mathbf{v}(\theta)^* \mathbf{H}\, \mathbf{v}(\theta), \quad \forall\, \theta, \tag{17}$$

$$\sum_{k=1}^{N} (a_k^2 + b_k^2) \le P_{\max}, \tag{18}$$

$$\mathbf{H} \succeq 0, \tag{19}$$

where the Melnikov Fourier coefficients entering $\mathcal{M}(\theta)$ are affine in (a_k, b_k) via (12)–(13). Constraint (17) together with $\mathbf{H} \succeq 0$ is the Fejér–Riesz certificate of Theorem 2 applied to the shifted polynomial $-\mathcal{M}(\theta) - \tau$, certifying that $-\mathcal{M}(\theta) \geq \tau$ for all θ.

Problem 2 (Min-power suppression)**.** Given a prescribed suppression margin $\tau_{\min} > 0$, find the forcing coefficients that minimize the total control power:

$$\min_{a_k, b_k, \mathbf{H}} \quad \sum_{k=1}^{N} (a_k^2 + b_k^2) \tag{20}$$

$$\text{s.t.} \quad -\mathcal{M}(\theta) - \tau_{\min} = \mathbf{v}(\theta)^* \mathbf{H}\, \mathbf{v}(\theta), \quad \forall\, \theta, \tag{21}$$

$$\mathbf{H} \succeq 0. \tag{22}$$

This is the dual design question to Problem 1: rather than maximizing robustness under a power constraint, we minimize the power required to achieve a prescribed level of robustness.

3.4 Certifying all homoclinic branches

The saddle in Assumption 1 may carry more than one homoclinic branch. The twin-well oscillator of Section 5 has a symmetric pair of loops forming a figure-eight, and the pendulum of Section 6 has upper and lower rotational separatrices. The Helmholtz escape oscillator of Section 7 instead carries a single homoclinic loop, since its other unstable branch escapes to infinity, so the certificate reduces to one block there. A transverse intersection along any branch produces a horseshoe, so suppression requires a sign-definite Melnikov function on every branch.

In the Duffing and Josephson examples the mirror branch is the odd image of the computed one, the response kernels change sign, and the damping contribution c_0 is invariant. With no DC bias the mirror Melnikov function satisfies $\mathcal{M}^-(\theta) = 2c_0 - \mathcal{M}(\theta)$, and sign-definiteness on both branches is the two-sided band

$$\tau \leq -\mathcal{M}(\theta) \leq 2|c_0| - \tau, \qquad \forall\, \theta, \tag{23}$$

certified by two Fejér–Riesz blocks that share the common constant term $|c_0| - \tau$. The synthesis problems remain semidefinite programs in the same decision variables. Writing $\mathcal{M} = c_0 + s(\theta)$ with s the zero-mean oscillatory part, the joint margin equals $|c_0| - \|s\|_\infty$: the two-branch max-margin design pins $-\mathcal{M}$ to $|c_0|$ in the Chebyshev sense, and full cancellation is optimal whenever the budget permits. With a nonzero DC bias the two branches carry different constant terms, and each branch polynomial is certified separately at the same cost.

All suppression designs reported in Sections 5 and 6 impose (23): Problems 1 and 2 carry a second Fejér–Riesz block, identical in size to the first, that certifies the mirror branch.

Remark 1 (Chaos induction). The same machinery can induce chaos rather than suppress it. Imposing $\mathcal{M}(\theta_1) \geq \gamma$ and $\mathcal{M}(\theta_2) \leq -\gamma$ at chosen phases θ_1, θ_2 with $\gamma > 0$ forces a sign change, and for generic parameters the resulting zeros are simple ($\mathcal{M}'(\theta^*) \neq 0$), so the Melnikov criterion gives transverse homoclinic intersections. Since $\mathcal{M}(\theta_i)$ is affine in (a_k, b_k), minimizing the power $\sum_k (a_k^2 + b_k^2)$ subject to these two linear constraints is a second-order cone program, and the dual maximizes γ at a fixed power budget. A transverse intersection yields a horseshoe, a chaotic invariant set that may be nonattracting, so induction guarantees complex transient dynamics rather than a chaotic attractor.

Remark 2 (Quasiperiodic forcing). The framework extends to quasiperiodic forcing with m incommensurate frequencies, where the Melnikov function becomes a multivariate trigonometric polynomial on $\mathbb{T}^m$ whose nonnegativity can be certified via block-Toeplitz positive semidefinite

matrices [21]. For $m \geq 2$ this certificate is sufficient but in general not necessary, so the exactness of the univariate Fejér–Riesz certificate, with no relaxation gap, is specific to the single-frequency case. A further extension concerns profile-shaping objectives, where $\mathcal{M}(\theta)$ is driven toward a target waveform while maintaining a definite sign; this yields a constrained least-squares problem that preserves convexity.

Remark 3 (Robust margins). Suppose $|\Delta c_0| \leq \rho_0$ and, independently, $|\Delta c_k| \leq \rho_k$, $|\Delta d_k| \leq \rho_k$ for $k \geq 1$. Then

$$\begin{aligned} |\Delta\mathcal{M}(\theta)| &\leq \rho_0 + \sum_{k=1}^{K} \rho_k(|\cos k\theta| + |\sin k\theta|) \\ &\leq \rho_0 + \sqrt{2}\sum_{k=1}^{K} \rho_k. \end{aligned}$$

Requiring the nominal margin to exceed the desired margin τ by $\rho_0 + \sqrt{2}\sum_k \rho_k$ therefore preserves the guarantee for every coefficient realization, with the same SDP structure. For a phase error $\Delta\phi_k$ in a Melnikov harmonic of amplitude $R_k = \sqrt{c_k^2 + d_k^2}$, the exact uniform change is $2R_k|\sin(\Delta\phi_k/2)| \leq R_k|\Delta\phi_k|$. The sum of these bounds gives a phase-error allowance directly, without replacing the correlated coefficient changes by independent boxes. A common timing error Δt gives $\Delta\phi_k = k\Omega\Delta t$. These bounds concern the specified coefficient or phase uncertainty, within the Melnikov approximation.

Remark 4 (Validity in ε). For a fixed design, the first-order splitting estimate is

$$d(t_0) = \frac{\varepsilon\,\mathcal{M}(\theta)}{|\mathbf{f}(\mathbf{z}_h(0))|} + O(\varepsilon^2).$$

A certified margin $\tau > 0$ keeps the splitting distance one-signed, and hence prevents intersections, for all ε below a threshold proportional to τ [1, 2]. The margin is therefore a quantitative buffer in the perturbation strength as well as in the forcing coefficients, provided the remainder is uniformly bounded. Its constant depends on the orbit and the selected forcing, so this estimate does not order the finite-ε robustness of different controllers by τ alone.

3.5 Peak-amplitude constraints

Some actuators limit the peak amplitude of the drive rather than its power. The control waveform $u(t) = \sum_{k=1}^{N}(a_k \cos k\Omega t + b_k \sin k\Omega t)$ is itself a trigonometric polynomial, so the bound $|u(t)| \leq u_{\max}$ for all t is the pair of nonnegativity conditions $u_{\max} \pm u(t) \geq 0$. Each is certified exactly by a Fejér–Riesz block of size $N + 1$, linear in (a_k, b_k), so a peak bound adds two positive semidefinite blocks and the synthesis stays a semidefinite program. This certifies the waveform peak exactly. The power budget alone gives only $\|u\|_\infty \leq \sum_k A_k \leq \sqrt{NP} = \sqrt{2N}\,u_{\mathrm{rms}}$, so it need not meet a separate peak-amplitude limit.

3.6 Comparison with existing control paradigms

To place our framework in context, we compare with three established approaches to chaos control, summarized in Table 1.

OGY closed-loop control [8] stabilizes unstable periodic orbits within an existing chaotic attractor via small parameter perturbations applied when the trajectory passes near the target orbit. It operates post hoc, requires real-time state measurement, and provides no global first-order certificate against homoclinic intersection.

Pyragas delayed feedback [9] applies a continuous control law $u(t) = K[x(t-T) - x(t)]$ to stabilize a periodic orbit of known period T. Like OGY, it requires continuous sensing and is further limited by the odd-number restriction in relevant system classes [24].

Single-harmonic open-loop forcing [4, 6] provides our numerical baseline. When the existing drive and the control both contain only the fundamental harmonic, the combined Melnikov function is $\mathcal{M}(\theta) = c_0 + R\cos(\theta - \psi)$. For $c_0 < 0$, the exact definite-sign condition is $R < |c_0|$. Optimizing amplitude and phase gives two Cartesian variables. If the existing drive contains higher harmonics, those terms remain in $\mathcal{M}$ even when the control has only one harmonic, and the full polynomial must be certified. Our $N = 1$ baseline optimizes both quadratures under that full certificate. Additional control harmonics can then reduce power or increase margin by shaping the residual terms.

This work provides open-loop, preventive control that prevents first-order homoclinic intersection rather than stabilizing within an existing chaotic attractor. The Fejér–Riesz certificate provides a global first-order guarantee (no relaxation gap within Melnikov theory), the Cartesian parametrization enables power-optimal allocation across N harmonics, the suppression margin τ serves as a quantitative margin certificate, and no real-time sensing is required, which is essential in environments where closing a feedback loop is impractical, such as MEMS devices at MHz frequencies or superconducting circuits in cryogenic conditions.

Table 1: Comparison of chaos control paradigms.

Feature	OGY	Pyragas	Single-harmonic	This work
Control type	Feedback	Feedback	Open-loop	Open-loop
Preventive vs. post-hoc	Post-hoc	Post-hoc	Preventive	Preventive
First-order guarantee	N/A	N/A	Yes (if feasible)	First-order (τ certificate)
Power-optimal	N/A	N/A	Within one harmonic	Across harmonics
Real-time sensing	Yes	Yes	No	No
Suppression certificate	No	No	Binary ($R < \lvert c_0\rvert$)	Quantitative (τ)

All guarantees in Table 1 are first-order in ε, valid within the Melnikov perturbative regime; see Section 10 for a discussion of this limitation. The primary quantitative baseline in our case studies is the optimal single-harmonic forcing under the same power budget, since it shares the same information structure (open-loop, supplementary, frequency-domain). Feedback methods operate under a fundamentally different information structure and are discussed for context rather than direct comparison.

3.7 Computational complexity

Both suppression problems (Problems 1 and 2) share the same $2N$ real decision variables $(a_k, b_k)_{k=1}^N$ (the Cartesian forcing coefficients) and are semidefinite programs. There is one Hermitian positive semidefinite block per certified branch. The Helmholtz example requires one block, while the two-branch band (23) for Duffing and Josephson requires two. Each block has size $(K+1) \times (K+1)$, where $K = \max(N_{\text{exist}}, N_{\text{ctrl}})$ is the highest harmonic present. The certificate degree follows the existing forcing, not the control count alone, so the single-harmonic ($N = 1$) rows of the tables below use 4×4 blocks. The chaos induction of Remark 1 requires no certificate matrix: the sign-change constraints are linear in (a_k, b_k) and the convex quadratic objective makes it a second-order cone program [23].

The exact reformulation has no nonconvex local optima. For a finite power budget, the max-margin problem attains its optimum; a feasible min-power problem also attains its minimum because its objective is coercive in the control coefficients. Standard conic algorithms solve these

programs to prescribed numerical accuracy under their usual regularity assumptions. In practice, the reported instances use CVXPy [25] with the CLARABEL solver and SCS as a fallback. The table times are recorded wall-clock solve-call durations, including canonicalization and the initial dense-grid check, below 0.05 s for the listed instances. They exclude subsequent plotting and simulations and vary with hardware. Since the control signal is designed offline and applied open-loop, the solve time is incurred once at the design stage, not at each control step. Numerical infeasibility status is subject to solver tolerances; the single-harmonic impossibility claim in Section 7 is established analytically.

4 Numerical Workflow and Validation Metrics

This section describes the computational pipeline used to solve the synthesis problems and validate the Melnikov predictions. All three case studies (MEMS resonator, Josephson junction, Helmholtz escape oscillator) share a common workflow: derive the response kernels κ_k^c, κ_k^s from the homoclinic orbit, solve the convex optimization program, and interpret the resulting Melnikov margin. Duffing and Josephson simulations use stroboscopic sections and Lyapunov exponents; the Duffing illustration additionally computes finite manifold segments in a common section. The Helmholtz illustration uses finite-horizon escape diagnostics. These tests assess the sampled trajectories and parameter ranges; they do not establish a global dynamical guarantee.

In each equation of motion, $d(t)$ denotes the existing periodic drive and $u(t)$ the supplementary control. For N_{ctrl} controllable harmonics,

$$u(t) = \sum_{k=1}^{N_{\mathrm{ctrl}}} \big[a_k \cos(k\Omega t) + b_k \sin(k\Omega t)\big].$$

Use of AI tools. OpenAI Codex assisted with revising manuscript text, preparing numerical verification and figure-generation code, checking reported results, and preparing submission files.

4.1 Homoclinic orbits and response kernels

For the three systems studied, closed-form expressions for the homoclinic orbits are available. The response kernels κ_k^c, κ_k^s are computed analytically using standard Fourier transforms [26, 27]. The nonzero kernels at $\Omega = 1$, $k = 1, \ldots, 10$, are checked by independent arbitrary-precision quadrature of the orbit velocities. We integrate on successive two-unit intervals over $[0, 100]$, use parity to recover the whole-line integral, and work at 45 decimal digits. A second calculation at 65 digits with cutoff 120 checks stability. The maximum relative discrepancy is below 10^{-20}; zero kernels vanish analytically by parity. Appendix A reports representative values and the explicit tail bounds.

4.2 SDP solver

Optimization problems are solved using CVXPy [25] with the CLARABEL interior-point solver, falling back to SCS at tolerance 10^{-9} when needed. Every returned design receives a dense-grid feasibility check on each relevant branch: two for Duffing and Josephson, one for Helmholtz. Sampling $-\mathcal{M}(\theta)$, and $-\mathcal{M}^-(\theta)$ when relevant, at 40,001 points requires each margin to meet the target to within 10^{-6}. These sampled checks detect numerical violations but do not replace the exact polynomial certificate. The timing includes the initial check within the solve call, while the final returned-value check is outside that timer. One case needs care: at the saturation margin $\tau_{\min} = \tau^*_{N=1}$ the single-harmonic min-power feasible set has empty interior, so we certify that instance with CLARABEL and report only the value that passes the dense-grid check.

4.3 Dynamical validation

We compare the first-order predictions with three nonlinear diagnostics. The revised diagnostics and their controller coefficients are saved separately from the optimization tables, with explicit numerical settings.

Poincaré sections. The full system (1) is integrated using `scipy.integrate.solve_ivp` with the DOP853 method at rtol = atol = 10^{-11} and maximum step $T/10$. Sampling at integer multiples of $T = 2\pi/\Omega$ gives a common stroboscopic section. Duffing sections discard 500 periods and retain 2 000 samples per initial condition, with newly computed two-branch max-margin controllers. Josephson sections discard 1 200 periods and retain 120 samples from each of three initial conditions; successive-point and pooled-radius checks verify convergence to a period-one response within 10^{-7}. Exact initial conditions and controller vectors accompany the saved data.

Manifold computation. We continue the Duffing saddle periodic orbit from $\varepsilon = 0$ to 0.25 in increments of 0.01 using shooting and the variational Jacobian. Its state monodromy matrix supplies the stable and unstable Floquet directions. Cubic local invariant-manifold parameterizations are advanced by two periods forward or backward; all plotted points therefore lie in the section $\Omega t = 0 \bmod 2\pi$. DOP853 uses relative tolerance 2×10^{-12} and absolute tolerance 2×10^{-13}. Adaptive refinement limits visible chords to 0.012 and midpoint interpolation errors to 2×10^{-5}. An extra-period, rescaled-seed check changes sampled curve points by less than 5×10^{-7}; tighter ODE tolerances change them by less than 2×10^{-10}. Finite traced segments do not establish global nonintersection.

Lyapunov and Floquet exponents. The largest state Lyapunov exponent is computed via the standard variational equation method [28]: the tangent linear equations are integrated simultaneously with the state, the tangent vector is renormalized every forcing period. Duffing estimates discard 300 periods and average 900, using relative and absolute tolerances 10^{-10} and maximum step $T/10$. The retained Duffing ε sweep uses these same settings. The retained Josephson forcing-stress scan discards 400 periods and averages 800 at the same tolerances. For the newly settled nominal Josephson periodic responses, we instead report the largest state Floquet exponent $\lambda_{\mathrm{F}} = T^{-1} \log \max_j |\mu_j|$, computed over one period with tolerances 10^{-12} and maximum step $T/40$. These state exponents exclude the neutral forcing-phase direction.

5 Case Study 1: MEMS Resonator (Duffing Framework)

Microelectromechanical resonators can exhibit Duffing-type nonlinearity from geometric stiffness and electrostatic effects [29]. High-frequency sensing and actuator bandwidth motivate considering an externally programmed drive. Here a normalized double-well Duffing model illustrates the synthesis principle; it is not calibrated to a specific MEMS device. We assume the supplementary waveform is phase-locked to the prescribed existing forcing. Actuator limits motivate a bound on the normalized forcing peak, which Section 3.5 certifies exactly. Translating that bound into a voltage limit or a pull-in guarantee requires an electrostatic force law, bias, total drive, and displacement constraints.

5.1 Equations and homoclinic orbit

The dynamics of the MEMS resonator with multiharmonic forcing is described by

$$\begin{aligned} \ddot{x} - x + x^3 &= \varepsilon[-\delta\dot{x} + d(t) + u(t)], \\ d(t) &= \sum_{k=1}^{N_{\mathrm{exist}}} \gamma_k \cos(k\Omega t), \end{aligned} \tag{24}$$

where $\delta = 0.80$ is the damping coefficient, $\Omega = 1.0$ is the forcing frequency, and $\varepsilon = 0.25$. The first summation represents the existing forcing that drives the system into chaos and cannot be modified; its amplitudes at harmonics $k = 1, 2, 3$ are $\gamma_1 = 1.20$, $\gamma_2 = 0.60$, $\gamma_3 = 0.32$. The multiharmonic structure of this perturbation reflects the spectral content of a drive signal that is not purely sinusoidal due to waveform distortion and/or nonlinear electrostatic coupling at the higher harmonics. The second summation is the supplementary control signal to be designed; its Cartesian coefficients (a_k, b_k) are the decision variables of the optimization. These parameters are chosen so that, in the absence of the control signal, the Melnikov function changes sign (predicting homoclinic chaos to first order) and the full nonlinear simulation confirms chaotic behavior (positive Lyapunov exponent), providing a meaningful test case for the suppression framework.

The unperturbed system $\ddot{x} - x + x^3 = 0$ has the Hamiltonian $H_0 = \dot{x}^2/2 - x^2/2 + x^4/4$ with a hyperbolic saddle at the origin and potential wells at $x = \pm 1$. The homoclinic orbit connecting the saddle to itself [1, 2] is described by

$$\begin{aligned} x_h(t) &= \sqrt{2}\,\mathrm{sech}(t), \\ \dot{x}_h(t) &= -\sqrt{2}\,\mathrm{sech}(t)\tanh(t). \end{aligned} \tag{25}$$

Since $\dot{x}_h(t)$ is odd, the response kernels (14)–(15) evaluate to

$$c_0 = -\frac{4\delta}{3} = -1.0667, \tag{26}$$

$$\kappa_k^c = 0, \quad \kappa_k^s = \frac{\sqrt{2}\,\pi k\Omega}{\cosh(\pi k\Omega/2)}, \tag{27}$$

where $\kappa_k^c = 0$ by parity (the integrand is odd) and κ_k^s follows from a standard residue calculation [26]. The kernel κ_k^s decays exponentially with k: $\kappa_1^s = 1.771$, $\kappa_2^s = 0.767$, $\kappa_3^s = 0.239$, $\kappa_5^s = 0.017$.

5.2 Uncontrolled Melnikov and sign changes

In the absence of the control signal, the three-harmonic perturbation produces the following Melnikov function:

$$\begin{aligned} \mathcal{M}_{\mathrm{unc}}(\theta) = &-1.067 + 2.125\sin\theta \\ &+ 0.460\sin 2\theta + 0.076\sin 3\theta, \end{aligned} \tag{28}$$

with $\min_\theta \mathcal{M}_{\mathrm{unc}} = -3.326$ and $\max_\theta \mathcal{M}_{\mathrm{unc}} = 1.193$. The sign change confirms that the uncontrolled system exhibits homoclinic chaos to first order; this is corroborated by the positive largest Lyapunov exponent $\lambda_{\max} = +0.16$ at $\varepsilon = 0.25$ (Fig. 4(a)).

5.3 Optimization results

Table 2 reports designs certified on both homoclinic branches. At $P_{\max} = 2.40$, the three-harmonic margin is 1.80 times the fundamental-only margin. The available budget permits the controller to cancel the three harmonics of the imposed drive exactly, attaining the upper bound $|c_0|$. Further harmonics cannot improve this maximum. At the matched margin $\tau_{\min} = \tau^*_{N=1} = 0.5940$, using three harmonics reduces the required power by 27%.

Fig. 1(a) shows the min-power Melnikov functions at matched margin $\tau_{\min} = \tau^*_{N=1}$: all three controlled curves lie within the band (23), touching the upper edge $\mathcal{M} = -\tau_{\min}$, but the $N = 3$ and $N = 5$ designs reach it with substantially less power ($P^* = 1.13$) than the single-harmonic design ($P^* = 1.54$). Fig. 1(b) shows the corresponding optimal control waveform for $N = 5$ over one

Table 2: MEMS/Duffing SDP results under the two-branch certificate (23). Max-margin column: optimal suppression margin τ^* under power budget $P_{\max} = 2.40$. Min-power column: optimal control power P^* at matched margin $\tau_{\min} = \tau^*_{N=1} = 0.5940$, so that every N is compared against the single-harmonic optimum.

N	Max-margin τ^*	Min-power P^*	$\tau^*/\tau^*_{N=1}$	$P^*/P^*_{N=1}$	Solve time (s)
1	0.5940	1.5401	1.00	1.00	0.014
2	0.9900	1.1285	1.67	0.73	0.023
3	1.0667	1.1263	1.80	0.73	0.017
5	1.0667	1.1254	1.80	0.73	0.029

forcing period. Fig. 2 shows the power-margin trade-off: at the nominal budget $P_{\max} = 2.40$, the $N = 3$ and $N = 5$ designs reach the maximum margin $|c_0| = 1.0667$ (full harmonic cancellation), while the $N = 1$ design saturates at $\tau^* = 0.5940$. Near the lower end of the plotted power range, a zero ordinate means that the design has no strictly positive certified margin. Fig. 3 summarizes the scaling with the number of harmonics: the minimum power saturates near $N = 3$ and the maximum margin plateaus at the cancellation limit, confirming that three harmonics capture essentially all the multiharmonic advantage in this case. Fig. 4 confirms the suppression through Poincaré sections: the chaotic scatter of the uncontrolled system (panel (a)) collapses to a single stable periodic orbit under all three controlled designs (panels (b)–(d)). Fig. 5 provides a separate geometric diagnostic using the $N = 5$ min-power controller at the matched margin. Three nontrivial uncontrolled intersections are numerically refined, with residuals below 10^{-10} and tangent angles above 30°. No nontrivial crossing is detected on the finite controlled segments; this observation supports, but does not prove globally, the first-order nonintersection prediction.

An actuator-amplitude limit motivates a peak bound, which Section 3.5 certifies exactly. The $N = 5$ max-margin design reaches the full-cancellation margin $|c_0| = 1.0667$ with a peak control amplitude $|u|_{\max} = 2.1200$. Imposing the illustrative bound $|u(t)| \le 1.5$ through the two extra Fejér–Riesz blocks caps the peak at exactly that value and still certifies a margin $\tau^* = 0.9878$, a small reduction from 1.0667. The peak constraint limits the supplementary waveform without changing the problem class. It does not by itself certify total-drive limits or electrostatic pull-in safety.

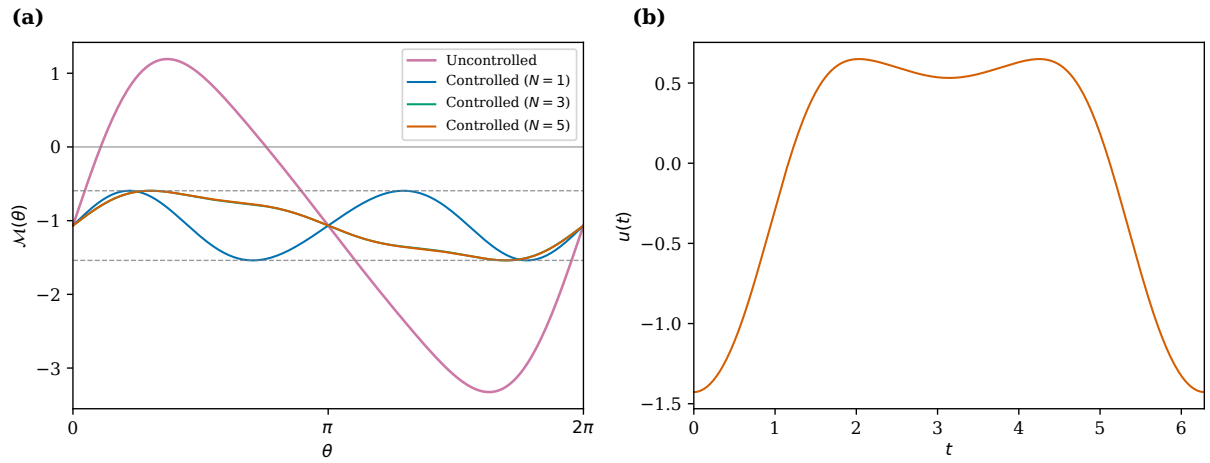

Figure 1: MEMS/Duffing case study. (a) Melnikov function: uncontrolled (sign changes predict homoclinic crossings to first order) vs. min-power controlled designs with $N = 1, 3, 5$ harmonics at matched margin $\tau_{\min} = \tau^*_{N=1} = 0.5940$; the dashed lines mark the band (23), within which all controlled curves are confined. (b) Optimal open-loop min-power control waveform $u(t)$ for $N = 5$ over one forcing period.

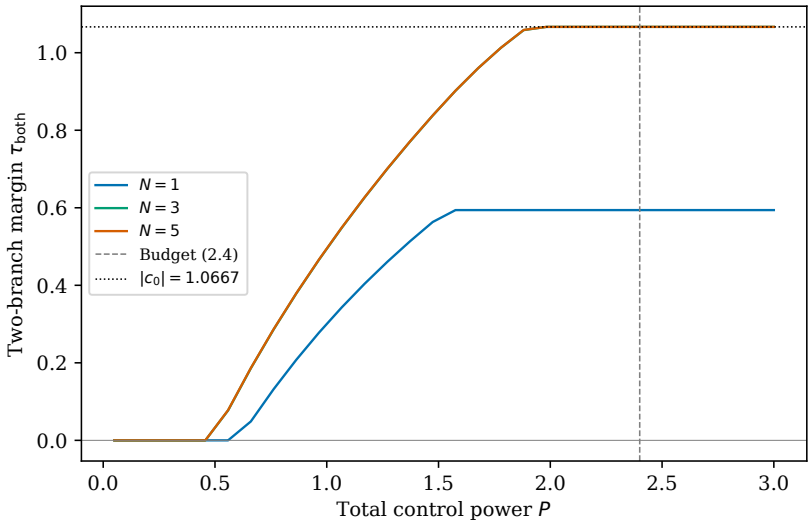

Figure 2: Duffing two-branch suppression margin versus control power P for $N = 1, 3, 5$. The curves show $\max(\tau^*, 0)$, so a zero ordinate indicates that strict suppression is uncertified. The vertical dashed line marks $P_{\max} = 2.40$. The horizontal dotted line marks the full-cancellation margin $|c_0| = 1.0667$.

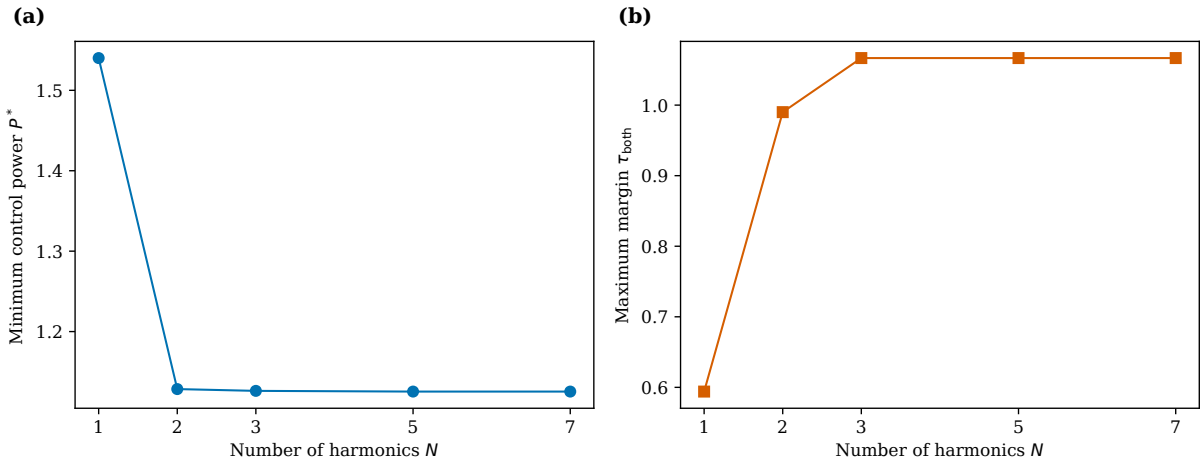

Figure 3: Performance scaling with number of harmonics. (a) Minimum control power P^* vs. N at matched margin $\tau_{\min} = \tau^*_{N=1} = 0.5940$. (b) Maximum margin τ^* vs. N at fixed power $P_{\max} = 2.40$. Both metrics show diminishing but clear returns from additional harmonics.

5.4 Robustness in the perturbation strength

The results above fix $\varepsilon = 0.25$. To probe validity over a range, we vary ε and recompute the largest Lyapunov exponent of the uncontrolled system and of the $N = 5$ controlled design (Fig. 6). The uncontrolled exponent turns positive near $\varepsilon = 0.25$ and stays positive above it, while the controlled exponent stays negative across $\varepsilon \in [0.05, 0.50]$: at the nominal $\varepsilon = 0.25$ it is -0.10 against $+0.16$ uncontrolled. Suppression therefore persists over a band of perturbation strengths, not a single point. This remains a one-parameter study, with the other parameters held at their nominal values.

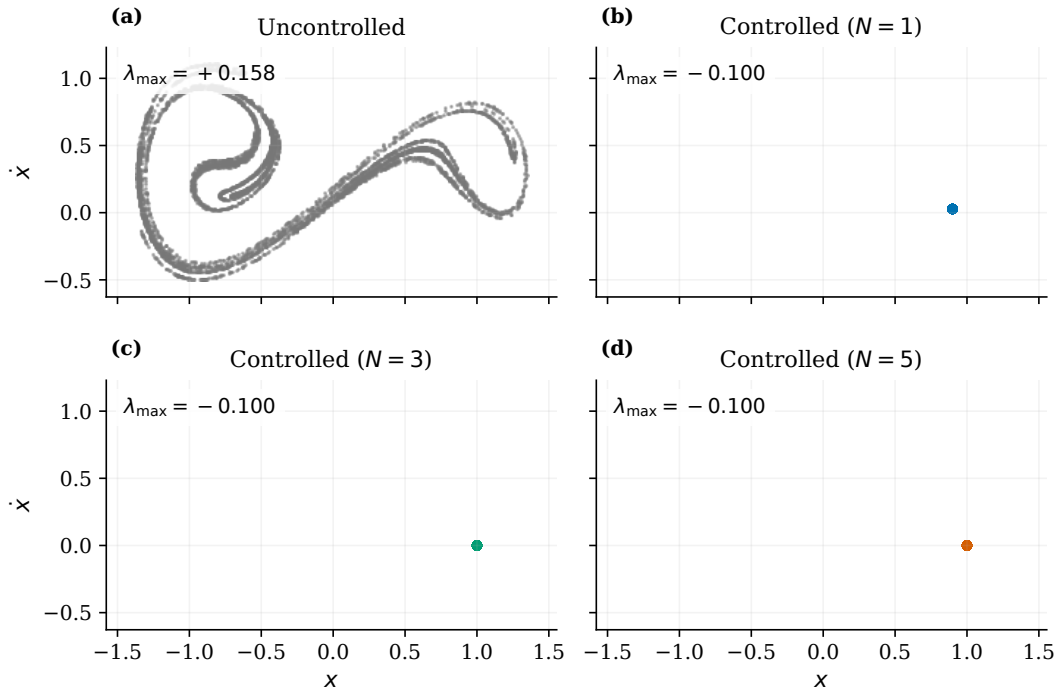

Figure 4: Poincaré sections for the Duffing oscillator at $\varepsilon = 0.25$. (a) Uncontrolled ($\lambda_{\max} = +0.16$, chaotic scatter). (b) $N = 1$ controlled. (c) $N = 3$ controlled. (d) $N = 5$ controlled. All three controlled designs regularize the dynamics; the single point in panels (b)–(d) indicates a stable periodic orbit. Larger N improves the Melnikov margin and suppression guarantee rather than changing the attractor type.

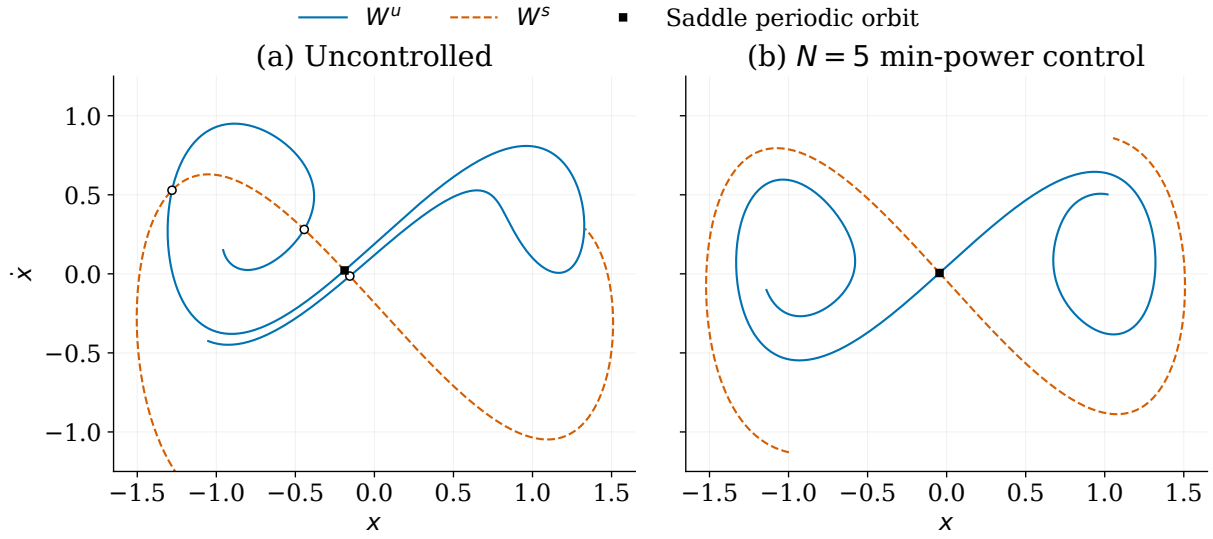

Figure 5: Stable (W^s, orange dashed) and unstable (W^u, blue solid) manifold segments of the Duffing stroboscopic map, all at $\Omega t = 0 \bmod 2\pi$. Black squares mark the saddle periodic orbit found by shooting; its Floquet directions seed the curves. (a) Uncontrolled: white circles mark numerically refined transverse intersections. (b) $N = 5$ two-branch min-power controller at $\tau_{\min} = 0.5940$: no nontrivial crossing is detected on the finite traced segments. The common saddle point is excluded from this comparison; no global nonintersection claim is made.

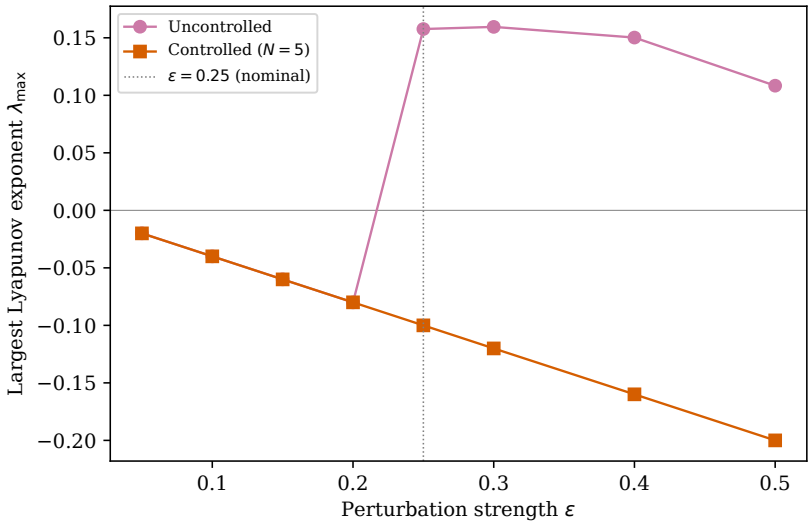

Figure 6: Duffing oscillator: largest Lyapunov exponent versus perturbation strength ε for the uncontrolled system and the $N = 5$ controlled design. The controlled exponent stays negative across the range, while the uncontrolled exponent is positive for $\varepsilon \gtrsim 0.25$.

6 Case Study 2: Josephson Junction

The dynamics of a current-biased Josephson junction under microwave irradiation are governed by the resistively and capacitively shunted junction (RCSJ) model [30, 31], which is mathematically identical to a damped driven pendulum [32]. The high-frequency cryogenic setting motivates externally programmed waveforms when readout, latency, or wiring constrain feedback. We assume a phase-locked supplementary drive transmitted through the same forcing channel. The example uses normalized parameters and does not establish the feasibility or necessity of open-loop control for a particular junction technology.

6.1 Equations and kernels

The RCSJ dynamics with multiharmonic forcing are described by

$$\begin{aligned} \ddot{\phi} + \sin\phi &= \varepsilon[-\alpha_d\dot{\phi} + I_{\mathrm{dc}} + d(t) + u(t)], \\ d(t) &= \sum_{k=1}^{N_{\mathrm{exist}}} [\gamma_k^c \cos(k\Omega t) + \gamma_k^s \sin(k\Omega t)], \end{aligned} \tag{29}$$

with damping $\alpha_d = 0.1$, no DC bias ($I_{\mathrm{dc}} = 0$), $\Omega = 1.0$, $\varepsilon = 0.1$, and existing drive with both cosine and sine components at harmonics $k = 1, 2, 3$: $\gamma_1^c = 0.30$, $\gamma_2^c = 0.25$, $\gamma_3^c = 0.20$, $\gamma_1^s = 0.20$, $\gamma_2^s = 0.15$, $\gamma_3^s = 0.10$. The mixed cosine/sine structure reflects a realistic microwave environment in which the ambient drive is not phase-aligned with a single reference.

The phase ϕ is defined modulo 2π. In a real-valued lift the upper separatrix connects $(-\pi, 0)$ to $(\pi, 0)$, which represent the same saddle on the phase cylinder. The lifted expression for this homoclinic orbit [32] is $\phi_h(t) = 4\arctan(e^t) - \pi$, $\dot{\phi}_h(t) = 2\,\mathrm{sech}(t)$. Since $\dot{\phi}_h(t)$ is even, the response kernels (14)–(15) evaluate to

$$\begin{aligned} \kappa_k^c &= \frac{2\pi}{\cosh(\pi k\Omega/2)}, \qquad \kappa_k^s = 0, \\ c_0 &= -8\alpha_d + 2\pi I_{\mathrm{dc}} = -0.800, \end{aligned} \tag{30}$$

with $\kappa_k^s = 0$ by parity and κ_k^c following from a standard residue calculation [26]. The kernel κ_k^c decays exponentially: $\kappa_1^c = 2.504$, $\kappa_2^c = 0.542$, $\kappa_3^c = 0.113$. Note the structural contrast with the Duffing case: here $\kappa_k^c \neq 0$ and $\kappa_k^s = 0$, reflecting the even parity of the homoclinic velocity.

6.2 Optimization results

Table 3 summarizes the SDP solutions under a tight normalized power budget $P_{\max} = 0.15$. Conversion of this illustrative budget to microwave power requires dimensional device parameters and a drive-line calibration.

Table 3: Josephson junction SDP results under the two-branch certificate (23). Max-margin column: optimal suppression margin τ^* under power budget $P_{\max} = 0.15$. Min-power column: optimal control power P^* at matched margin $\tau_{\min} = \tau^*_{N=1} = 0.6358$.

N	Max-margin τ^*	Min-power P^*	$\tau^*/\tau^*_{N=1}$	$P^*/P^*_{N=1}$	Solve time (s)
1	0.6358	0.1358	1.00	1.00	0.014
3	0.7004	0.1258	1.10	0.93	0.017
5	0.7004	0.1258	1.10	0.93	0.038

The multiharmonic designs achieve a 10% larger suppression margin than the single-harmonic baseline at fixed power, and a 7% power saving at matched margin, with both branches certified. The optimal fundamental-only controller nearly cancels both quadratures of the first harmonic. The residual fundamental cosine and sine drive coefficients are -0.00618 and -0.00501, respectively. Retaining these small terms improves the worst-case margin in the presence of the uncontrolled second and third harmonics. At these parameters the uncontrolled system has a regular attracting response in the sampled simulations, despite the Melnikov sign change. The latter predicts a nonattracting horseshoe for sufficiently small ε; it does not prove its persistence at the finite perturbation strength simulated here.

Fig. 7(a) shows the Melnikov functions under the max-margin controlled designs: the $N = 1$ curve retains visible oscillation, while the $N = 3$ and $N = 5$ curves are flatter around the same fixed average c_0, reflecting the additional Fourier degrees of freedom used to counteract the mixed cos/sin existing drive. Fig. 8 shows the power-margin trade-off: up to $P \approx 0.13$, all three designs track each other closely; beyond that point, single-harmonic control saturates near $\tau^* \approx 0.6358$, while multiharmonic control continues to improve toward the full-cancellation limit $|c_0| = 0.800$.

6.3 Dynamical validation

Fig. 9 shows Poincaré sections and largest state Floquet exponents for the uncontrolled system and the $N = 1$ and $N = 3$ two-branch designs at the nominal parameters. The attractor is a regular periodic orbit in every sampled case, with largest state Floquet exponent approximately -0.005 in the nominal tests. A regular sampled attractor is compatible with the first-order homoclinic-crossing prediction, which need not describe an attracting chaotic set. Section 8 reports the first-order forcing thresholds; no positive-exponent threshold was detected in the sampled Josephson stress range, so a nonlinear improvement is not inferred there.

7 Case Study 3: Helmholtz Escape Oscillator

The Helmholtz oscillator is the standard archetype for capsize by escape from a potential well [33, 34]. A vessel rolling in beam seas sits in a safe basin around the upright position, and a

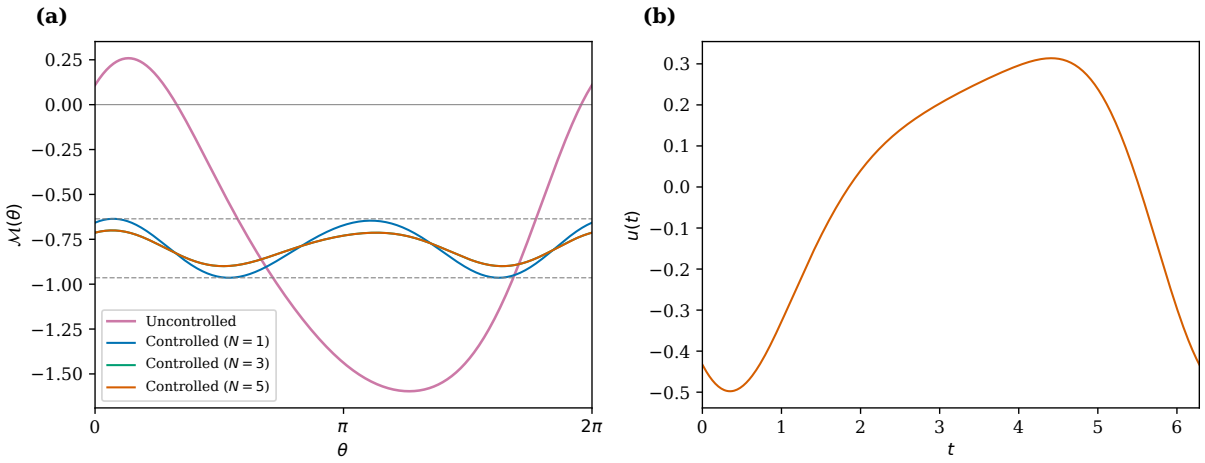

Figure 7: Josephson junction. (a) Melnikov function: uncontrolled vs. max-margin controlled designs with $N = 1, 3, 5$ under power budget $P_{\max} = 0.15$. (b) Optimal control waveform $u(t)$ for $N = 5$ over one forcing period.

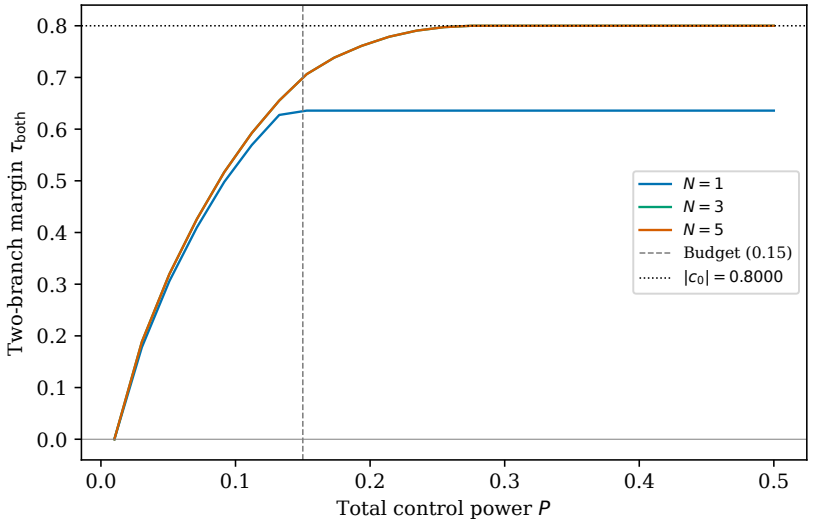

Figure 8: Josephson two-branch suppression margin versus control power P for $N = 1, 3, 5$. The curves show $\max(\tau^*, 0)$, so a zero ordinate indicates that strict suppression is uncertified. The vertical dashed line marks $P_{\max} = 0.15$. At larger budgets the multiharmonic designs approach $|c_0| = 0.800$, while the fundamental-only design saturates at 0.6358.

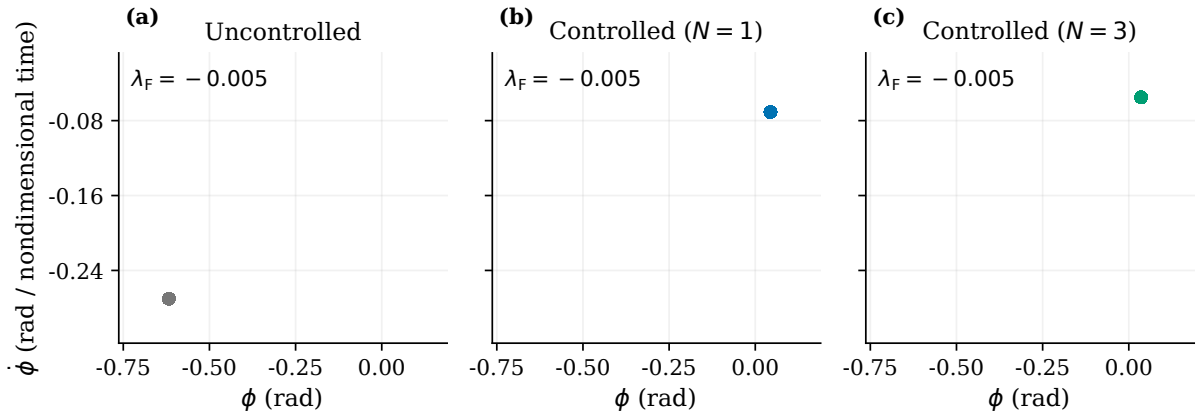

Figure 9: Josephson junction: settled Poincaré sections from three initial conditions, plotted on common axes, and largest state Floquet exponents λ_{F} for the uncontrolled system and the $N = 1$ and $N = 3$ two-branch designs. All sampled initial conditions settle to a period-one response at the nominal parameters.

large wave can drive it across the angle of vanishing stability, past which the righting moment no longer restores the upright state and the vessel capsizes. Periodic forcing erodes the safe basin by creating a homoclinic tangle at the escape saddle, so a Melnikov criterion again governs the onset of the erosion, and suppressing the predicted tangle can reduce basin erosion. This illustration assumes a deterministic periodic excitation with known phase and a synchronized supplementary drive. A sea spectrum alone does not provide this phase information; application to irregular seas requires additional modeling and uncertainty treatment. This case study also connects the framework to the optimal-excitation line of Lenci and Rega [14], who studied homoclinic control of the same escape oscillator.

7.1 Model and kernels

The non-dimensional roll angle ϕ satisfies

$$\begin{aligned} \ddot{\phi} + \phi - \phi^2 &= \varepsilon[-\delta\dot{\phi} + d(t) + u(t)], \\ d(t) &= \sum_{k=1}^{N_{\mathrm{exist}}} \gamma_k \sin(k\Omega t), \end{aligned} \tag{31}$$

with hydrodynamic damping $\delta = 0.10$, encounter frequency $\Omega = 1.0$, $\varepsilon = 0.1$, and wave excitation amplitudes $\gamma_1 = 0.10$, $\gamma_2 = 0.30$, $\gamma_3 = 0.15$. The upright state $\phi = 0$ is a center, and the saddle at $\phi = 1$ marks the angle of vanishing stability. The homoclinic orbit that bounds the safe basin is

$$\begin{aligned} \phi_h(t) &= 1 - \tfrac{3}{2}\operatorname{sech}^2(t/2), \\ \dot{\phi}_h(t) &= \tfrac{3}{2}\operatorname{sech}^2(t/2)\tanh(t/2). \end{aligned} \tag{32}$$

This saddle carries a single homoclinic loop; the other unstable branch escapes to infinity, so one certificate block suffices here, in contrast with the figure-eight and pendulum cases of Section 3.4. Since $\dot{\phi}_h(t)$ is odd, the response kernels (14)–(15) evaluate to

$$\begin{aligned} &\kappa_k^c = 0, \qquad \kappa_k^s = -\frac{6\pi(k\Omega)^2}{\sinh(\pi k\Omega)}, \\ &c_0 = -\tfrac{6}{5}\delta = -0.12, \end{aligned} \tag{33}$$

with $\kappa_k^c = 0$ by parity and κ_k^s following from a standard residue calculation [26]: $\kappa_1^s = -1.6322$, $\kappa_2^s = -0.2816$, $\kappa_3^s = -0.0274$. For these parameters the third-harmonic response is about one sixtieth of the fundamental response.

The sine wave excitation produces cosine terms in the Melnikov function,

$$\begin{aligned}\mathcal{M}_{\mathrm{unc}}(\theta) = & -0.12 + 0.1632\cos\theta \\ & + 0.0845\cos 2\theta + 0.0041\cos 3\theta,\end{aligned} \tag{34}$$

with range $[-0.2398, 0.1318]$. The Melnikov function takes both signs. Direct integration provides the finite-time escape measurements in Fig. 11.

7.2 Optimization results

Table 4 reports the max-margin designs under the normalized power budget $P_{\max} = 0.06$. Control at the fundamental frequency yields $\tau^* = 0.0355$. Adding the second harmonic raises the margin to 0.0982, approximately 2.8 times the fundamental-only value. The $N = 3$ and $N = 5$ margins agree with the $N = 2$ value to the reported precision at this budget. Exact cancellation of all three drive harmonics requires power 0.1225 and yields the upper bound $|c_0| = 0.12$.

Table 4: Helmholtz escape oscillator, max-margin designs under budget $P_{\max} = 0.06$. τ^*: suppression margin on the single homoclinic loop.

N	Max-margin τ^*	$\tau^*/\tau^*_{N=1}$
1	0.0355	1.00
2	0.0982	2.77
3	0.0982	2.77
5	0.0982	2.77

The min-power problem exposes a sharper separation. We set the ambitious target $\tau_{\min} = \frac{2}{3}|c_0| = 0.08$, and Table 5 reports the minimum power that certifies it. The single-harmonic program is infeasible, with an elementary analytic obstruction independent of the numerical solver. Write the residual polynomial as

$$\begin{aligned}\mathcal{M}(\theta) = & \, c_0 + C_1\cos\theta + D_1\sin\theta \\ & + C_2\cos 2\theta + C_3\cos 3\theta,\end{aligned}$$

where a first-harmonic controller changes only C_1, D_1; $C_2 = -\gamma_2\kappa_2^s$ and $C_3 = -\gamma_3\kappa_3^s$ are fixed. Since $[\mathcal{M}(0) + \mathcal{M}(\pi)]/2 = c_0 + C_2$, every such controller obeys

$$\tau = -\max_\theta \mathcal{M}(\theta) \le |c_0| - C_2 \simeq 0.0355 < 0.08. \tag{35}$$

This upper bound is attained: choosing $C_1 = -C_3$, $D_1 = 0$ gives $\mathcal{M} = c_0 + C_2 - \sin^2\theta(2C_2 + 4C_3\cos\theta)$, whose maximum is $c_0 + C_2$ because $C_2 \ge 2|C_3|$ for these parameters. The associated power is $P = 0.0105$. Control restricted to the fundamental therefore cannot attain the target at any power. Adding the second harmonic makes the target feasible at $P^* = 0.0355$ (rounded).

In Fig. 10(a), the maximum of the fundamental-only Melnikov function lies above the target line $\mathcal{M} = -0.08$. The two- and three-harmonic designs remain below it at every phase. In panel (b), the $N = 1$ margin reaches its ceiling near 0.0355. The $N = 2$ and $N = 3$ curves reach 0.0982 at $P = 0.06$. At $P = 0.1225$ the $N = 3$ design cancels all three drive harmonics and attains $\tau^* = |c_0| = 0.12$, which it retains at higher budgets.

Table 5: Helmholtz escape oscillator, min-power designs at the target $\tau_{\min} = \frac{2}{3}|c_0| = 0.08$. The fundamental-only design is infeasible at every power level.

N	Min-power P^*
1	infeasible
2	0.0355
3	0.0355
5	0.0355

In the Duffing and Josephson comparisons, the prescribed target equals the optimal fundamental-only margin at the nominal budget. Additional harmonics can therefore be compared by the power they save at that target. In the Helmholtz comparison, the chosen target 0.08 exceeds the fundamental-only ceiling set by the fixed second-harmonic coefficient C_2 in (35). The drive spectrum and response kernels determine these residual coefficients. The power budget and the location of the target relative to the ceiling determine which comparison can be made.

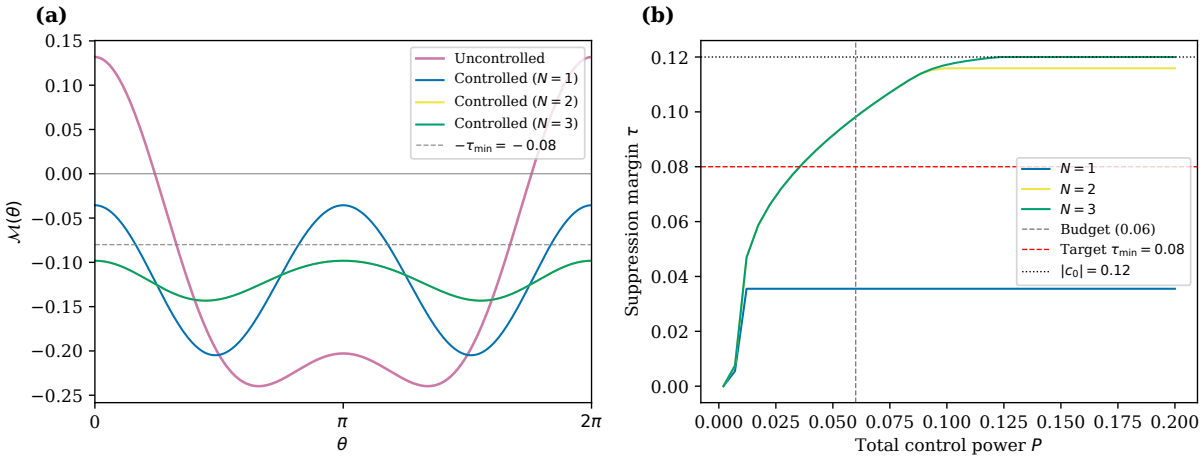

Figure 10: Helmholtz escape oscillator. (a) Uncontrolled and optimized Melnikov functions at $P_{\max} = 0.06$. The dashed line marks $\mathcal{M} = -0.08$. (b) Suppression margin versus power, shown as $\max(\tau^*, 0)$. A zero ordinate indicates that strict suppression is uncertified. The fundamental-only ceiling is approximately 0.0355. Two harmonics reach the target 0.08 (red dashed line), and three harmonics reach $|c_0| = 0.12$ at $P = 0.1225$.

7.3 Safe-basin integrity

We assess escape using a finite-horizon survival diagnostic. Scaling the excitation by $\kappa \geq 1$, we integrate a 13×13 grid of initial conditions in $[-0.6, 0.9] \times [-0.6, 0.6]$ for 120 forcing periods. A trajectory is classified as escaped when it crosses $\phi = 1.5$ or exceeds $|\phi| = 1.5$. DOP853 uses relative and absolute tolerances 10^{-6} and maximum step T. The fraction surviving this test estimates finite-horizon basin integrity on that grid, rather than an infinite-time safe basin or a capsize probability. Fig. 11 compares the uncontrolled system with the $N = 2$ controlled design. Its sampled survival fraction is larger at the tested forcing scales: at $\kappa = 4$ the uncontrolled fraction is 37% of the sampled grid while the controlled design retains 46%. The phase-plane pictures use a finer 30×30 grid over the same rectangle and horizon.

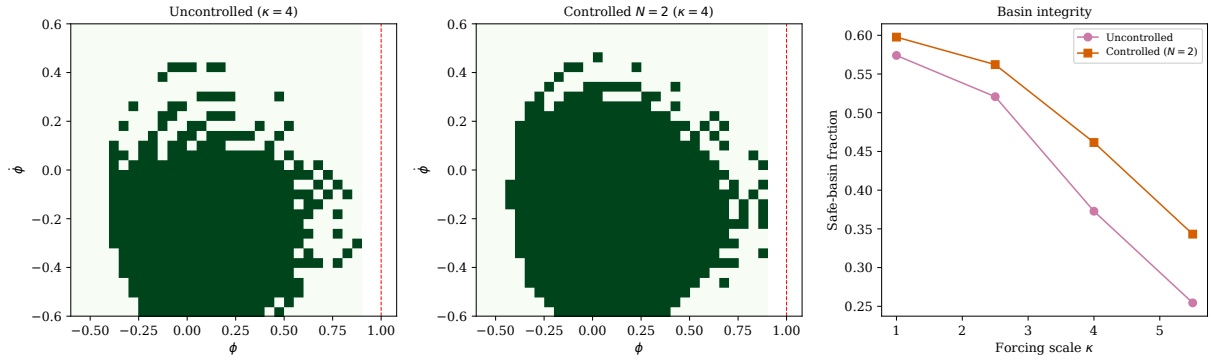

Figure 11: Helmholtz escape oscillator, safe-basin integrity under a forcing scale κ. (a) Uncontrolled and (b) $N = 2$ controlled 120-period survival sets (green) at $\kappa = 4$; the red line marks the unperturbed saddle $\phi = 1$. (c) Sampled survival fraction versus κ; these finite-grid observations do not certify infinite-time basin boundaries.

7.4 Benchmark against Lenci and Rega

Lenci and Rega [15] solved the same shaping problem for this oscillator by a variational argument. They maximize the minimum over phase of the normalized Melnikov oscillatory part $\cos\theta + \sum_{k=2}^{N} f_k \cos k\theta$, with the fundamental fixed at unit amplitude, and report the gain G_N, the ratio of the critical excitation amplitude of the shaped drive to that of the pure harmonic. This is the Fejér–Riesz program in one block: minimizing the constant t that keeps $t + \cos\theta + \sum_{k=2}^{N} f_k \cos k\theta \geq 0$ gives $G_N = 1/t$. Table 6 compares their reported gains with the semidefinite program. The gains agree to four decimals for $N \leq 5$. At $N = 6$, the saved comparison is 1.8476 versus 1.8478, a difference of 2×10^{-4} that is retained explicitly in the table. The auxiliary problem minimizes t subject to affine coefficient constraints and an exact nonnegativity certificate, so its optimal value is global. Agreement with the published gains is an independent numerical benchmark; it does not establish uniqueness of the waveform. The single-superharmonic optimum is $G_2 = \sqrt{2}$, the two-superharmonic optimum is the golden ratio $G_3 = \varphi$, and the sequence approaches the theoretical bound $G_\infty = 2$.

The Lenci–Rega benchmark fixes the fundamental amplitude and optimizes a single-loop gain. For the power-limited problem in Section 7, we instead bound the sum of squared control coefficients and impose a uniform Melnikov margin. The same nonnegativity certificate also permits a peak-amplitude bound (Section 3.5) and, with one matrix block per branch, a shared control waveform for the two-branch examples (Section 3.4).

Table 6: Validation against Lenci and Rega [15], Table 1: comparison of optimal gains G_N for the Helmholtz oscillator with N harmonics. $G_{\mathrm{L\&R}}$ is their reported value, G_{SDP} the Fejér–Riesz program. The $N = 6$ discrepancy is displayed without asserting equality. The theoretical bound is $G_\infty = 2$.

N	$G_{\mathrm{L\&R}}$	G_{SDP}
2	1.4142	1.4142
3	1.6180	1.6180
4	1.7321	1.7321
5	1.8019	1.8019
6	1.8476	1.8478

8 The Suppression Margin as a Robustness Buffer

The margin has a precise coefficient-space interpretation: a nominal certificate with margin τ survives any additive Melnikov error whose uniform norm is below τ, on every certified branch. For forcing scaling, write the existing oscillatory contribution as $F_{\text{exist}}(\theta)$ and hold the controller fixed. The bound $(\kappa - 1)\|F_{\text{exist}}\|_\infty < \tau$ is sufficient for retaining the sign certificate. The actual band-closing scale also depends on the phase profile of the residual waveform.

For each design, we compute that first-order scale from the scaled Melnikov coefficients, and compare it with a finite simulation scan. For Duffing and Josephson, the scan detects the first sampled interval where the estimated Lyapunov exponent exceeds 0.02, then interpolates linearly; it does not locate the first strictly positive exponent. The forcing-scale increment is 0.15. Duffing is scanned through $\kappa = 2.95$ and Josephson through $\kappa = 3.40$. For Helmholtz, a 0.5-step scan through $\kappa = 6$ locates a 15% reduction of the 120-period survival fraction relative to its value at $\kappa = 1$, with linear interpolation. These operational thresholds depend on the initial conditions, grid, horizon, and numerical settings.

Fig. 12 plots both against the certified margin τ. The first-order thresholds increase between $N = 1$ and $N = 3$ for Duffing and Josephson, and between $N = 1$ and $N = 2$ for Helmholtz. They are not strictly monotone across every design: Duffing's $N = 2$ threshold is slightly above its $N = 3$ threshold. Duffing's simulated threshold decreases from approximately 2.08 at $N = 1$ to 1.97 at $N = 3$, even though its certified margin increases. No sampled Josephson exponent exceeds 0.02 through $\kappa = 3.40$; those results are censored rather than measured transitions. The detected nonlinear thresholds lie beyond the first-order ones in these tests, but neither a general ordering of controllers nor global dynamical robustness follows from the margin alone.

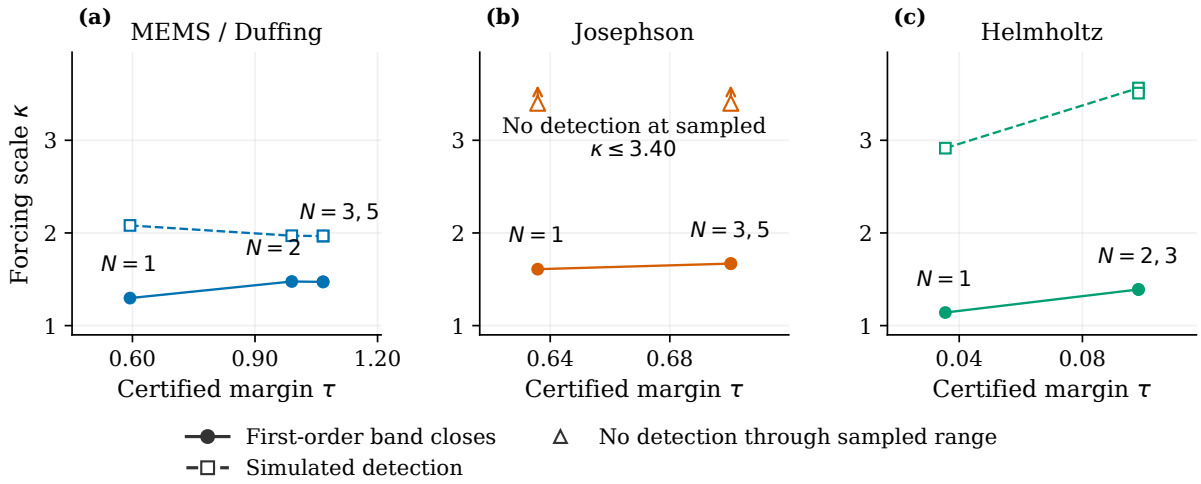

Figure 12: Critical forcing scale κ_{crit} versus certified margin τ for all designs. Solid marks: first-order critical scale, where the certified band closes. Open marks: interpolated simulation thresholds under the stated scan criteria. Josephson results are censored at the largest sampled forcing scale. A larger margin certifies a larger uniform additive-error allowance, but need not increase the nonlinear forcing threshold.

9 One-Branch versus Two-Branch Certification

Table 7 makes the two-branch correction explicit for the twin-well and pendulum case studies. The single-branch program certifies a margin $\tau^{(1)}$ on the computed loop alone. Evaluated on a dense grid, the same design leaves an actual mirror-branch margin τ^- that is potentially smaller,

so a single-branch value can overstate the guarantee. The two-branch max-margin program (23) certifies τ_{both} at the fixed case-study power budget. A separate min-power solve gives P_{both} at the common target $\tau_{\min} = \tau^*_{N=1}$. The two columns generally describe different controllers. The multiharmonic advantage survives the correction in both systems.

Table 7: One-branch versus two-branch certification for the twin-well and pendulum case studies. $\tau^{(1)}$: margin certified by the single-branch program. τ^-: the actual mirror-branch margin of that design, from a 40,001-point grid. τ_{both}: maximum margin certified on both branches at the fixed power budget. P_{both}: minimum control power at the separate matched target $\tau_{\min} = \tau^*_{N=1}$, rather than at the displayed max-margin value.

System	N	$\tau^{(1)}$	τ^-	τ_{both}	P_{both}
MEMS/Duffing	1	0.6067	0.3807	0.5940	1.5401
	2	0.9900	0.9900	0.9900	1.1285
	3	1.0667	1.0667	1.0667	1.1263
	5	1.0667	1.0667	1.0667	1.1254
Josephson	1	0.6420	0.6017	0.6358	0.1358
	3	0.7142	0.6326	0.7004	0.1258
	5	0.7142	0.6326	0.7004	0.1258

10 Discussion and Limitations

Several limitations of the framework should be stated clearly.

Open-loop structure. The control signal is designed offline and applied without feedback, so there is no adaptation to unmodeled disturbances or slow parameter drift. The suppression margin τ provides a built-in buffer: a design with $\tau \gg 0$ tolerates moderate parameter deviations before the Melnikov function changes sign. The designer can size this buffer explicitly by solving the max-margin problem at a power budget calibrated to the anticipated uncertainty, but if actual parameters deviate sufficiently from their nominal values, the design may fail silently.

Perturbative regime. The entire framework rests on the first-order Melnikov approximation, valid in the small-ε regime. As ε increases, higher-order terms in the manifold splitting become significant and the first-order predictions degrade. At $\varepsilon = 0.25$, the controlled Duffing trajectories tested here have negative largest state Lyapunov exponents ($\lambda_{\max} \approx -0.100$) and converge to periodic responses (Fig. 4(b)–(d)). These trajectory-level observations complement the perturbative certificate. When ε exceeds the perturbative regime, the SDP design provides a principled initial guess that can be refined by numerical continuation or direct optimization in the full nonlinear system.

Scalability. The polynomial degree is $K = \max(N_{\text{exist}}, N_{\text{ctrl}})$. There is one $(K+1) \times (K+1)$ Hermitian block per certified homoclinic branch, plus two $(N_{\text{ctrl}}+1)$-dimensional blocks when peak constraints are imposed. Scalability beyond the small instances reported here has not been benchmarked. Solver accuracy, conditioning, computational resources, and independently realizable actuator harmonics all limit the usable design size.

Data-driven extensions. The case studies exploit closed-form homoclinic orbits and analytical response kernels. For systems where closed-form expressions are unavailable, the kernels can in principle be estimated from numerical integration of the homoclinic orbit or from trajectory data. Developing data-driven kernel estimation with quantified uncertainty is a natural direction for future work.

Stochastic perturbations. Stochastic forcing requires a separate splitting analysis with the noise scaling, stochastic-calculus convention, and observation horizon specified [2, 35]. A pointwise Gaussian quantile does not bound the supremum of a random Melnikov process over all phases or times. If such an analysis supplies a uniform error bound η with a stated confidence, the deterministic certificate can be tightened by η. Establishing that probabilistic bound and its range of validity is future work; no stochastic suppression confidence is claimed here.

11 Conclusion

For a fixed set of phase-locked control harmonics, we have formulated two first-order design problems as semidefinite programs. One maximizes the uniform signed Melnikov margin at fixed power. The other minimizes power at a prescribed margin. Cartesian harmonic coefficients make the Melnikov polynomial affine in the control, and the Fejér–Riesz certificate enforces the margin at every phase on each specified homoclinic branch. The related problem of inducing a sign change at prescribed phases admits a second-order cone formulation.

The three case studies quantify what the additional harmonics make possible. In Duffing and Josephson, multiharmonic forcing reduces the power required for the matched two-branch margin by 27% and 7%, respectively. In the single-loop Helmholtz oscillator, the multiharmonic margin is approximately 2.8 times the fundamental-only margin at $P = 0.06$. The analytic bound (35) gives a sharp fundamental-only ceiling of approximately 0.0355, while two harmonics attain the target 0.08. The reported solve-call times are below 0.05 s for the tabulated designs, including the initial numerical feasibility check.

Several directions remain for future work. Experimental validation on MEMS resonators or Josephson junction platforms would test the framework beyond the perturbative simulations presented here. Data-driven estimation of response kernels from trajectory data, using sparse identification techniques [36], would extend the framework to systems without closed-form homoclinic orbits. Finally, integrating the offline SDP design with a slow adaptive feedback loop that updates the open-loop waveform as parameters drift would combine the global guarantees of the Melnikov approach with the adaptivity of closed-loop methods.

Statements and Declarations

Funding. No specific funding supported this work.

Competing interests. The author declares no competing financial or nonfinancial interests.

Data and code availability. Online Resource 1 contains the numerical data, Python scripts, and instructions for reproducing the optimization results, figures, and numerical checks reported in this article.

A Closed-Form Response Kernels

This appendix collects the analytical derivations of the damping coefficient c_0 and the response kernels κ_k^c, κ_k^s for each case study. The nonzero response kernels and damping integrals are checked with arbitrary-precision orbit quadrature as described in Section 4; representative values appear in Table 8.

A.1 MEMS/Duffing oscillator

The homoclinic orbit is $x_h(t) = \sqrt{2}\,\mathrm{sech}(t)$, $y_h(t) = -\sqrt{2}\,\mathrm{sech}(t)\tanh(t)$. Since the perturbation enters through the velocity equation, the area form reduces to $\omega(\mathbf{f}, \mathbf{g}) = y_h(t) \cdot g_y$, where g_y is the y-component of the perturbation. The damping coefficient follows from

$$\begin{aligned} c_0 &= -\delta \int_{-\infty}^{\infty} y_h^2(t)\, dt \\ &= -2\delta \int_{-\infty}^{\infty} \mathrm{sech}^2(t)\tanh^2(t)\, dt = -\frac{4\delta}{3}. \end{aligned} \tag{36}$$

For the response kernels, $y_h(t)$ is odd, so $\int_{-\infty}^{\infty} y_h(t)\cos(k\Omega t)\, dt = 0$ (integrand odd), giving $\kappa_k^c = 0$. The sine integral evaluates by residue calculus [26] to

$$\begin{aligned} &\int_{-\infty}^{\infty} \mathrm{sech}(t)\tanh(t)\sin(k\Omega t)\, dt \\ &\qquad = \pi k\Omega\ \mathrm{sech}\left(\frac{\pi k\Omega}{2}\right), \end{aligned} \tag{37}$$

yielding $\kappa_k^s = \sqrt{2}\,\pi k\Omega/\cosh(\pi k\Omega/2)$.

A.2 Josephson junction / pendulum

The homoclinic orbit is $\phi_h(t) = 4\arctan(e^t) - \pi$, $\dot{\phi}_h(t) = 2\ \mathrm{sech}(t)$. Since $\dot{\phi}_h(t)$ is even, the sine integral vanishes by parity, giving $\kappa_k^s = 0$. The cosine integral evaluates by residue calculus [26] to

$$\int_{-\infty}^{\infty} \mathrm{sech}(t)\cos(k\Omega t)\, dt = \pi\ \mathrm{sech}\left(\frac{\pi k\Omega}{2}\right), \tag{38}$$

yielding $\kappa_k^c = 2\pi/\cosh(\pi k\Omega/2)$.

The damping coefficient combines the dissipation and DC bias contributions:

$$\begin{aligned} c_0 = &-\alpha_d \int_{-\infty}^{\infty} \dot{\phi}_h^2(t)\, dt + I_{\mathrm{dc}} \int_{-\infty}^{\infty} \dot{\phi}_h(t)\, dt \\ = &-8\alpha_d + 2\pi I_{\mathrm{dc}}, \end{aligned} \tag{39}$$

where the first integral evaluates to $4\int_{-\infty}^{\infty}\mathrm{sech}^2(t)\, dt = 8$ and the second to $\phi_h(\infty) - \phi_h(-\infty) = \pi - (-\pi) = 2\pi$, the net phase advance around the separatrix.

A.3 Helmholtz escape oscillator

The homoclinic orbit of $\ddot{\phi} + \phi - \phi^2 = 0$ about the saddle at $\phi = 1$ is $\phi_h(t) = 1 - \frac{3}{2}\mathrm{sech}^2(t/2)$, $\dot{\phi}_h(t) = \frac{3}{2}\mathrm{sech}^2(t/2)\tanh(t/2)$. Since $\dot{\phi}_h(t)$ is odd, $\int_{-\infty}^{\infty}\dot{\phi}_h(t)\cos(k\Omega t)\, dt = 0$ (integrand odd), giving $\kappa_k^c = 0$. Integrating by parts with $\frac{d}{dt}\mathrm{sech}^2(t/2) = -\mathrm{sech}^2(t/2)\tanh(t/2)$ and the standard transform [26] $\int_{-\infty}^{\infty}\mathrm{sech}^2(x)\cos(cx)\, dx = \pi c/\sinh(\pi c/2)$ gives

$$\begin{aligned} &\int_{-\infty}^{\infty} \mathrm{sech}^2(t/2)\tanh(t/2)\sin(k\Omega t)\, dt \\ &\qquad = \frac{4\pi(k\Omega)^2}{\sinh(\pi k\Omega)}, \end{aligned} \tag{40}$$

Multiplying this integral by the velocity prefactor $3/2$ gives $\kappa_k^s = -6\pi(k\Omega)^2/\sinh(\pi k\Omega)$. The damping coefficient is

$$\begin{aligned} c_0 &= -\delta \int_{-\infty}^{\infty} \dot{\phi}_h^2(t)\, dt \\ &= -\frac{9}{4}\delta \int_{-\infty}^{\infty} \operatorname{sech}^4(t/2) \tanh^2(t/2)\, dt \\ &= -\frac{6}{5}\delta. \end{aligned} \tag{41}$$

The single homoclinic loop of this saddle needs one certificate block, in contrast with the twin-well and pendulum cases.

For the nonzero Fourier integral truncated at $|t| \le L$, the omitted tail is bounded in absolute value by $4\sqrt{2}e^{-L}$ (Duffing), $8e^{-L}$ (Josephson), and $12e^{-L}$ (Helmholtz), using elementary bounds on the respective velocities. At $L = 100$, all three are below 5×10^{-43}. The 45-digit calculation and an independent 65-digit, $L = 120$ calculation agree to relative error below 10^{-20} for all 30 nonzero kernels with $k = 1, \ldots, 10$. These are numerical quadrature checks with analytic tail bounds, rather than interval arithmetic certificates.

Table 8: Representative nonzero response kernels at $\Omega = 1$. The numerical column integrates the orbit velocity at 45-digit precision with cutoff $|t| \le 100$. All 30 checked nonzero kernels ($k = 1, \ldots, 10$ in each system) have relative discrepancy below 10^{-20} from the analytical expressions. Zero kernels vanish by parity.

System	k	Kernel	Analytical	Quadrature
Duffing	1	κ_k^s	1.770652417	1.770652417
Duffing	3	κ_k^s	0.239450939	0.239450939
Duffing	5	κ_k^s	0.017247411	0.017247411
Duffing	10	κ_k^s	$1.339100268 \times 10^{-5}$	$1.339100268 \times 10^{-5}$
Josephson	1	κ_k^c	2.504080663	2.504080663
Josephson	3	κ_k^c	0.112878255	0.112878255
Josephson	5	κ_k^c	0.004878305	0.004878305
Josephson	10	κ_k^c	$1.893773760 \times 10^{-6}$	$1.893773760 \times 10^{-6}$
Helmholtz	1	κ_k^s	-1.632174330	-1.632174330
Helmholtz	3	κ_k^s	-0.027380701	-0.027380701
Helmholtz	5	κ_k^s	$-1.420330320 \times 10^{-4}$	$-1.420330320 \times 10^{-4}$
Helmholtz	10	κ_k^s	$-8.561849318 \times 10^{-11}$	$-8.561849318 \times 10^{-11}$

B Fejér–Riesz Certificate (Proof Sketch)

Proof of Theorem 2. (Necessity.) Let $T(\theta) = \sum_{k=-N}^{N} \hat{c}_k e^{\mathrm{i}k\theta}$ be a nonnegative trigonometric polynomial of degree N. By the Fejér–Riesz theorem, there exists an algebraic polynomial $p(z) = \sum_{j=0}^{N} p_j z^j$ such that $T(\theta) = |p(e^{\mathrm{i}\theta})|^2$ for all θ. Expanding the squared modulus gives

$$T(\theta) = \sum_{j,\ell=0}^{N} p_j \overline{p_\ell}\, e^{\mathrm{i}(j-\ell)\theta} = \mathbf{v}(\theta)^* \mathbf{H}\, \mathbf{v}(\theta), \tag{42}$$

where $\mathbf{H} = \overline{\mathbf{p}}\, \mathbf{p}^\top$ with $\mathbf{p} = [p_0, \ldots, p_N]^\top$. Since $\mathbf{H}$ is an outer product of rank at most one, $\mathbf{H} \succeq 0$. Matching Fourier coefficients on both sides yields the diagonal-offset sum constraints (9).

More generally, any $\mathbf{H} \succeq 0$ satisfying (9) produces a valid representation (it need not have rank one). The feasible set is the intersection of the positive semidefinite cone with the affine subspace defined by (9), which is convex by construction.

(*Sufficiency.*) Conversely, if $\mathbf{H} \succeq 0$ satisfies (9), then $\mathbf{v}(\theta)^{*}\mathbf{H}\,\mathbf{v}(\theta) \geq 0$ for all θ by positive semidefiniteness, and expanding the quadratic form recovers $T(\theta)$ by the diagonal-offset sum constraints. Hence $T(\theta) \geq 0$. □

See Dumitrescu [21] for a comprehensive treatment of positive trigonometric polynomials and their semidefinite representations, and Grenander and Szegő [22] for the classical theory of Toeplitz forms.

References

[1] Guckenheimer, J., Holmes, P.: Nonlinear Oscillations, Dynamical Systems, and Bifurcations of Vector Fields. Springer, New York (1983). https://doi.org/10.1007/978-1-4612-1140-2

[2] Wiggins, S.: Introduction to Applied Nonlinear Dynamical Systems and Chaos, 2nd edn. Springer, New York (2003). https://doi.org/10.1007/b97481

[3] Smale, S.: Differentiable dynamical systems. Bulletin of the American Mathematical Society **73**(6), 747–817 (1967) https://doi.org/10.1090/S0002-9904-1967-11798-1

[4] Lima, R., Pettini, M.: Suppression of chaos by resonant parametric perturbations. Physical Review A **41**(2), 726–733 (1990) https://doi.org/10.1103/PhysRevA.41.726

[5] Braiman, Y., Goldhirsch, I.: Taming chaotic dynamics with weak periodic perturbations. Physical Review Letters **66**(20), 2545–2548 (1991) https://doi.org/10.1103/PhysRevLett.66.2545

[6] Chacón, R.: Melnikov method approach to control of homoclinic/heteroclinic chaos by weak harmonic excitations. Philosophical Transactions of the Royal Society A **364**(1846), 2335–2351 (2006) https://doi.org/10.1098/rsta.2006.1828

[7] Chacón, R.: Control of Homoclinic Chaos by Weak Periodic Perturbations. World Scientific, Singapore (2005). https://doi.org/10.1142/5001

[8] Ott, E., Grebogi, C., Yorke, J.A.: Controlling chaos. Physical Review Letters **64**(11), 1196–1199 (1990) https://doi.org/10.1103/PhysRevLett.64.1196

[9] Pyragas, K.: Continuous control of chaos by self-controlling feedback. Physics Letters A **170**(6), 421–428 (1992) https://doi.org/10.1016/0375-9601(92)90745-8

[10] Shinbrot, T., Grebogi, C., Yorke, J.A., Ott, E.: Using small perturbations to control chaos. Nature **363**, 411–417 (1993) https://doi.org/10.1038/363411a0

[11] Preciado, V.M., Chacón, R.: A novel polynomial method for taming chaos in a wide class of nonlinear oscillators. In: Proceedings of the 2003 International Conference on Physics and Control, vol. 2, pp. 390–395. IEEE, Piscataway, NJ (2003). https://doi.org/10.1109/PHYCON.2003.1236855

[12] Chacón, R., Preciado, V., Tereshko, V.: Suppressing temporal and spatio-temporal chaos by multiple weak resonant excitations: Application to arrays of chaotic coupled oscillators. Europhysics Letters **63**(5), 667–673 (2003) https://doi.org/10.1209/epl/i2003-00582-9

[13] Preciado, V.M., Verghese, G.C.: Suppression of homoclinic chaos using multiharmonic inputs: Melnikov analysis and root-locus design. Conference presentation listed in the final program of the 6th IFAC Symposium on Nonlinear Control Systems (NOLCOS 2004), session 6.3, September 3, Stuttgart, Germany (2004). https://web.archive.org/web/20060515181401/http://www.nolcos2004.uni-stuttgart.de/?site=1#os6

[14] Lenci, S., Rega, G.: Optimal control of nonregular dynamics in a Duffing oscillator. Nonlinear Dynamics **33**, 71–86 (2003) https://doi.org/10.1023/A:1025509014101

[15] Lenci, S., Rega, G.: Optimal control of homoclinic bifurcation: theoretical treatment and practical reduction of safe basin erosion in the Helmholtz oscillator. Journal of Vibration and Control **9**(3–4), 281–315 (2003) https://doi.org/10.1177/107754603030753

[16] Cao, H., Chen, G.: Global and local control of homoclinic and heteroclinic bifurcations. International Journal of Bifurcation and Chaos **15**(8), 2411–2432 (2005) https://doi.org/10.1142/S0218127405013393

[17] Chacón, R.: Maintenance and suppression of chaos by weak harmonic perturbations: a unified view. Physical Review Letters **86**(9), 1737–1740 (2001) https://doi.org/10.1103/PhysRevLett.86.1737

[18] Zambrano, S., Mariño, I.P., Salvadori, F., Meucci, R., Sanjuán, M.A.F., Arecchi, F.T.: Phase control of intermittency in dynamical systems. Physical Review E **74**(1), 016202 (2006) https://doi.org/10.1103/PhysRevE.74.016202

[19] Melnikov, V.K.: On the stability of the center for time-periodic perturbations. Transactions of the Moscow Mathematical Society **12**, 1–57 (1963)

[20] Fejér, L.: Über trigonometrische Polynome. Journal für die reine und angewandte Mathematik **146**, 53–82 (1916) https://doi.org/10.1515/crll.1916.146.53

[21] Dumitrescu, B.: Positive Trigonometric Polynomials and Signal Processing Applications. Springer, Dordrecht (2007). https://doi.org/10.1007/978-1-4020-5125-8

[22] Grenander, U., Szegő, G.: Toeplitz Forms and Their Applications. University of California Press, Berkeley, CA (1958). https://doi.org/10.1525/9780520355408

[23] Boyd, S., Vandenberghe, L.: Convex Optimization. Cambridge University Press, Cambridge (2004). https://doi.org/10.1017/CBO9780511804441

[24] Nakajima, H.: On analytical properties of delayed feedback control of chaos. Physics Letters A **232**, 207–210 (1997) https://doi.org/10.1016/S0375-9601(97)00362-9

[25] Diamond, S., Boyd, S.: CVXPY: A Python-embedded modeling language for convex optimization. Journal of Machine Learning Research **17**(83), 1–5 (2016)

[26] Gradshteyn, I.S., Ryzhik, I.M.: Table of Integrals, Series, and Products, 7th edn. Academic Press, Amsterdam (2007). https://www.sciencedirect.com/book/9780123736376/table-of-integrals-series-and-products

[27] Abramowitz, M., Stegun, I.A.: Handbook of Mathematical Functions with Formulas, Graphs, and Mathematical Tables. Dover, New York (1965)

[28] Benettin, G., Galgani, L., Giorgilli, A., Strelcyn, J.-M.: Lyapunov characteristic exponents for smooth dynamical systems and for Hamiltonian systems: a method for computing all of them. part 1: Theory. Meccanica **15**(1), 9–20 (1980) https://doi.org/10.1007/BF02128236

[29] Rhoads, J.F., Shaw, S.W., Turner, K.L.: Nonlinear dynamics and its applications in micro- and nanoresonators. Journal of Dynamic Systems, Measurement, and Control **132**(3), 034001 (2010) https://doi.org/10.1115/1.4001333

[30] McCumber, D.E.: Effect of ac impedance on dc voltage-current characteristics of superconductor weak-link junctions. Journal of Applied Physics **39**(7), 3113–3118 (1968) https://doi.org/10.1063/1.1656743

[31] Stewart, W.C.: Current-voltage characteristics of Josephson junctions. Applied Physics Letters **12**(8), 277–280 (1968) https://doi.org/10.1063/1.1651991

[32] Strogatz, S.H.: Nonlinear Dynamics and Chaos: With Applications to Physics, Biology, Chemistry, and Engineering, 2nd edn. Westview Press, Boulder, CO (2015). https://doi.org/10.1201/9780429492563

[33] Thompson, J.M.T., Soliman, M.S.: Fractal control boundaries of driven oscillators and their relevance to safe engineering design. Proceedings of the Royal Society of London A **428**, 1–13 (1990) https://doi.org/10.1098/rspa.1990.0022

[34] Falzarano, J.M., Shaw, S.W., Troesch, A.W.: Application of global methods for analyzing dynamical systems to ship rolling motion and capsizing. International Journal of Bifurcation and Chaos **2**(1), 101–115 (1992) https://doi.org/10.1142/S0218127492000100

[35] Simiu, E.: Chaotic Transitions in Deterministic and Stochastic Dynamical Systems: Applications of Melnikov Processes in Engineering, Physics, and Neuroscience. Princeton University Press, Princeton, NJ (2002). https://doi.org/10.1515/9781400832507

[36] Brunton, S.L., Proctor, J.L., Kutz, J.N.: Discovering governing equations from data by sparse identification of nonlinear dynamical systems. Proceedings of the National Academy of Sciences **113**(15), 3932–3937 (2016) https://doi.org/10.1073/pnas.1517384113